Heliyon 10 (2024) e25199

Contents lists available at ScienceDirect

Heliyon

journal homepage: www.cell.com/heliyon

Research article

Prediction of phase composition and mechanical properties Fe–Cr–C–B–Ti–Cu hardfacing alloys: Modeling and experimental Validations

Vasyl Lozynskyi [a,b], Bohdan Trembach [c,*], Md Mukter Hossain [d], Mohammad Humaun Kabir [e], Yury Silchenko [c], Michal Krbata [f], Kostiantyn Sadovyi [g], Oleksii Kolomiitse [h], Liubomyr Ropyak [i]

[a] *Belt and Road Initiative Centre for Chinese-European Studies (BRICCES), Guangdong University of Petrochemical Technology, Maoming, 525000, China*
[b] *Department of Mining Engineering and Education, Dnipro University of Technology, 49005, Dnipro, Ukraine*
[c] *Private Joint Stock Company, Novokramatorsky Mashinostroitelny Zavod, 84305, Ukraine*
[d] *Department of Physics, Chittagong University of Engineering and Technology (CUET), 4349, Chittagong, Bangladesh*
[e] *Department of Materials Science and Engineering, Chittagong University of Engineering and Technology (CUET), 4349, Chittagong, Bangladesh*
[f] *Alexander Dubcek University of Trenčín, 911 06, Trenčín, Slovakia*
[g] *Armament Department of the Radio-Technical Troops, Ivan Kozhedub Kharkiv National Air Force University, 61023, Kharkiv, Ukraine*
[h] *Department of Computing Engineering and Programming, National Technical University Kharkiv Polytechnic Institute, 61000, Kharkiv, Ukraine*
[i] *Department of Computerized Mechanical Engineering, Ivano-Frankivsk National Technical University of Oil and Gas, 15 Karpatska Str., 76019, Ivano-Frankivsk, Ukraine*

ARTICLE INFO

Keywords:
Coating
Hardfacing
Deposited metal
Fe–C–B–Cr–Ti alloy
Phase diagram
DFT
CASTEP
Mechanical properties

ABSTRACT

Alloys of the Fe–Cr–C–B–Ti alloy system are characterized by brittleness, which can be eliminated by the copper alloy, while corrosion resistance and abrasive wear resistance are significantly reduced. In this article, comprehensive investigations are carried out on the microstructure and mechanical properties of the proposed high-copper boron-containing alloy 110Cr4Cu7Ti1VB. Systematic theoretical and experimental studies encompassed thermodynamic calculations in ThermoCALC, production of flux-cored wires for hardfacing and welding, receipt of SEM images, acquisition of load and unload diagrams (discharge) via instrumental indentation on various phases of the deposited metal, and determination of chemical composition at indentation points through local chemical analysis. Mechanical properties of some phases such as γ–Fe phase (austenite), hemioboride $Fe_2(B,C)$ and boron cementite $Fe_3(B,C)$ and titanium carbide TiC in Fe–Cr–C–B–Ti–Cr alloy were determined by using density functional theory (DFT) implemented in the CASTEP code. We also compared these compounds; properties with other available commercial compounds, where available. With the knowledge of calculated elastic constants, the moduli, the Pugh's modulus ratio G/B, the Poisson's ratio v and the hardness of the title phases, 110Cr4Cu7Ti1VB were further predicted and discussed.

* Corresponding author.
E-mail addresses: lvg.nmu@gmail.com (V. Lozynskyi), btrembach89@gmail.com (B. Trembach), mukter_phy@cuet.ac.bd (M.M. Hossain), mkhumaun@gmail.com (M.H. Kabir), sua6163430@gmail.com (Y. Silchenko), michal.krbata@tnuni.sk (M. Krbata), igor-krasnij@ukr.net (K. Sadovyi), Alexus_k@ukr.net (O. Kolomiitse), l_ropjak@ukr.net (L. Ropyak).

https://doi.org/10.1016/j.heliyon.2024.e25199
Received 26 September 2023; Received in revised form 5 January 2024; Accepted 23 January 2024
Available online 5 February 2024

1. Introduction

Mining industry is one of the branches characterized by significant energy consumption. In the world economy growth conditions, the rising of prices for energy resources, slow transition of the economies of developed countries to renewable energy sources (solar, wind, etc.) led the world economy to energy crisis. According to the statistics, around 23% of global energy consumption and roughly 80% of wear and wear-related failure stem from friction [1]. In addition, the wear of individual parts leads to a gradual decrease in performance, efficiency and work parameters of a machines and complexes. Considering into account the constantly growing requirements, it is necessary to increase the efficiency and effectiveness of technological processes, machines and vehicles [2]. The theoretical foundations of healing crack-like defects in structures using repair coatings and patches were developed for cracked plates [3–5] and shells [6–9]. The effect of injections of non-contrast filler on the strength of bodies with through and surface defects is studied in articles [10,11].

For these reasons, increasing the wear resistance parts and machine parts used in the mining industry is a recent problem; thus, effective and inexpensive solutions are needed [12]. Wear resistance can be increased due to the use of surfacing technology [13–17]. In addition, due to replacing of worn-out components and the associated down times are costly. Before welding coatings, due attention should be paid to the preparation of the surfaces of machine parts [18]. According to the condition of filler material deposition, the three most popular surfacing techniques utilized today are as follows: solution state (sole gel, electrochemical deposition [19,20], chemical solution deposition), gaseous state (ion beam-assisted deposition (IBAD), chemical vapour deposition (CVD)), physical vapour deposition (PVD) [21,22] and molten or semi-molten state (arc welding, plasma technology [23,24], spraying [25–28] and laser/electron beam [29,30]. Another issue is the shaping properties of surface layers to improve the tribological characteristic and wear resistance by various surface engineering methods including heat treatment [31,32] and thermochemical treatment (oxidation [33,34], carburizing, boriding, nitriding [35]) etc. Among the variety of methods used for hardening coating applications, the simplest and most efficient are the arc welding techniques [2,36,37]. Of the different surfacing techniques, hardface welding has the greatest mobility, process flexibility, and thickness-building ability [38]. The following welding techniques are widely implemented in practice [39,40]: shielded metal arc welding (SMAW) [41,42], gas tungsten arc welding (GTAW [43,44] or TIG) [45,46], gas metal arc welding (GMAW or MIG), submerged arc welding (SAW), manual metal arc welding (MMA or MMAW) and flux-cored arc welding (FCAW) [2, 14,47–51]. Self-shielded flux-cored wires arc welding (FCAW–S) is more environmentally friendly and more energy efficiency [52], higher productivity, high quality of the deposited metal, high deposition rate, arc visibility [41,48,49]. The flux cored wires segment is the most significant by type segment in the global market, and is expected to be the first preference [52].

The main aspect influencing the parts renovation hardening durability and the choice of hardfacing (welding) technology, is the choice of deposited metal type. High chromium Fe–Cr–C alloys system is the most widely used alloy [53], because in view of high volumetric share of carbide precipitations (M_7C_3, M_3C_2 and $M_{23}C_6$ [54,55]. But high chromium Fe–Cr–C alloys deposited metal alloys are easy to crack in the process of hardfacing, which imposes limitations on their application [56]. The tendency to cracking is explained by the large shrinkage of the deposited metal during cooling, prevented by the substrate (thermal stress). The formation of cracks helps to release a portion of thermal stress, but there is still a considerable amount of residual thermal stress inside [57]. As a result, a significant level of thermal stress inside the overlay is accumulated, often higher than its material strength, leading to cracks uniformly distributed over the whole overlay plate [36]. Residual stresses can later lead to cracking during operation through the formation of chips [58]. Thus, it is necessary to increase the ability to the deposited metal internal stresses relief, which can be achieved primarily by regulation of the main alloying elements content (reducing of the carbide phase content), as well as additional alloying by increasing ductility elements. Anyway it will lead to abrasive wear resistance decreasing. In addition, it is necessary to reduce the cost of filler materials and improve the hardfacing process efficiency In this connection, Fe–C–B system alloys being highly resistant to abrasive wear and having relatively low cost, become more widely spread [59,60]. Today, there are numerous investigations into simple ternary alloys of the Fe–C–B system [61–64], as well as additionally alloyed with a carbide-forming element [25,65–67] such as Cr [41,68–70], V, Nb, Mo [71,72], Ti [47,73], ferrite forming element (Al, Si) [58,73] and austenite forming element [74] (Cu [75,76], Ni, Mn). Boron can form the following compounds in these alloys: iron monoboride FeB, hemioboride Fe_2B, $Fe_3(B,C)$ and cubic boron carbide $Fe_{23}(C,B)_6$. In most cases, most part of the boron will form the hemiboride Fe_2B, being a brittle phase. The latter is explained by inherent brittleness of Fe_2B due to the week B–B bond along [002] direction [77,78], which leads to a great susceptibility of boron alloys to cracking. Kirkovska et al. [79] showed that among the alloying elements C, Cr, Mn, V, W, Mn + V, the greatest increase in the indentation modulus of both monoboride FeB and hemioboride Fe_2B, was observed in alloying with chromium. Whereas the lowest modulus in the case of FeB formed in Fe–B–X (X = C, Cr, Mn) was measured in the presence of C as an alloying element, while for Fe_2B, in Mn alloyed Fe_2B. It explains the interest of modern researchers to Fe–C–Cr–B alloys. It is necessary to limit the carbon and manganese content. Depending on the content of elements in Fe–C–Cr–B system alloys, carbides, borides and carboborides can be formed in the alloys. Studies by Lentz et al. [68] Fe–C–Cr–B alloys alloys showed that the fracture toughness as well as hardness of M_2B phase can simultaneously be increased by purposely adjusting the Cr content (up to 5 mass%) [80,81]. Mechanical properties increasing can be explained by the structure of hemioboride Fe_2B, which is rearranged from an orthogonal lattice to a tetragonal one [64]. At that, Fe_2B with a tetragonal lattice is less brittle. Further improvement of the mechanical properties of hemioboride due to additional alloying of the boride [67,79] elements (Ti, V, Cr, Co, Ni, and Cu) showed that it can enhance the ductility of the Fe_2B, but cannot change the intrinsic brittle nature of the Fe_2B [67]. Copper increases the plastic properties of hemioboride most of all the range of alloying elements M = Ti, V, Cr, Mn, Co, Ni and Cu $(Fe_{0.875}M_{0.125})_2B$, at the same time, the value of G/B (0.5883) is close to the critical value of the ductile/brittleness transition (0.571) [67]. In addition, V and Ni have a greater effect on mechanical properties than Ti and Cr [67]. The experimental works suggested that Cr, Mn and Mo increase the hardness of Fe_2B,

whereas Ni and Cu reduce it [82–86]. Moreover, Cr, Mn, Mo and Cu have shown the capability for reducing the brittleness of Fe_2B In this case, further improvement of alloys performances can be achieved due to the improvement of the matrix mechanical characteristics [67,82,84,86].

Particularities of materials with a heterogeneous structure of the surface layer foresee an interaction of soft matrix and solid phase in the process of elastic and plastic deformation. The matrix connects and holds the solid phase, therefore the alloy wear resistance depends on its mechanical properties [87,88]. If the matrix strength is insufficient, it is squeezed out (INDENTION) at stresses above the yield point of the matrix, due to the occurrence of a high level of plastic deformations in the plastic matrix. The latter causes the strengthening phase microcracking (carbides, borides, etc.), due to the lack of the matrix mechanical support [89,90]. In this case, the matrix properties, namely its hardness and plasticity, play a decisive role in solid phase cracking prevention. The matrix properties are determined by the degree of its carburization and saturation by alloying elements, its structure, as well as the dispersion and the second phase rate (two- and multiphase structures). Copper is part of the bonds in composite materials [91]. Thus, some studies have shown [92,93], that two- or multi-phase steels with relatively lower hardness can have significantly increased resistance to abrasive wear due to a good combination of strength and ductility compared to the martensite high strength. Thus, Yoo et al. [94], engaged in study of the abrasive wear of boron-containing steels, came to the conclusion that alloys with a relatively low boron content (less than 0.6%) had better wear resistance compared to metals with a higher boron content (more than 1%). A decrease in resistance to abrasive wear of steels containing a larger amount of boron (more than 1%) is also connected with the formation of a brittle FeB phase and a small amount of residual austenite [94]. Ductility of austenitic matrix is greater then of the martensitic phase. So it's to be expected that the deposited metal cracking resistance (brittle failure mechanism) will be increased. The results showed [95], that an addition of Mn and Cr can increase the Fe_2B ductile and significantly intensify an interaction between metal matrix and strengthening phase. Austenite phase increasing can be achieved by adding of austenite-forming elements such as Ni or Cu. Copper is almost not dissolved in cementite and chromium carbides [96,97], and also does not form compounds with boron (B) and remains only in the matrix [98]. A copper is mostly dissolved in austenite, thereby it has influence to the formation of residual austenite in Fe–B–C–Cu alloys [99,100], formation of the martensitic phase and prevents the ferrite and pearlite formation [99,101]. It should also be noted that with the addition of copper the solubility of carbon in the matrix decreases [102]. In addition, it is known that copper increases the strength of steel i [103]. It was found the Cu precipitates can effectively improve strength without harm to toughness [104]. The Cu-precipitates also can reduce the mobility of dislocations [105]. Dislocation would loop around the nondeformable precipitates, which is beneficial for toughness [106]. Thus, the deposited metals with Cu addition are necessary to study, and the welding consumables with suitable Cu addition is an efficient solution for an advanced strength-toughness balance [103]. Yi et al. [76] studied the effect of Cu on the microstructure, mechanical properties and wear resistance of Fe–Cr–B–C alloy. The composite coatings with different Cu additions were mainly composed of α–Fe, γ–Fe, M_2B and $M_{23}(C,B)_6$. With the increase of Cu additions, the coating matrix structure gradually changed from pearlite to martensite, and hard phases of M_2B and $M_{23}(C,B)_6$. The results showed that appropriate addition of Cu improved the hardness and impact toughness of the alloy, and wear resistance increased with the increase of Cu contents [107].

Flux-cored wire electrode consists of the outer metal shell and core filler. When flux-cored wire is used, the required chemical composition of the deposited metal is provided mostly by the filler composition. One of the main issues during hardfacing processes, is to ensure the deposited metal required performance indicators (composition, mechanical properties, abrasion and corrosion resistance, etc.) as well as the required quality of the deposited metal [108–112]. Many researchers propose the introduction of an exothermic addition into welding materials [2,48,52,113–116]. as a solution for the energy efficiency and productivity increasing. It allowed to reduce a consumption of electricity used for welding materials melting due to a chemical heat generation. According to research, an introduction of exothermic addition in the core filler is an effective measure to improve the uniformity of flux-cored wire melting [48, 117,118]. Besides, the introduction of an exothermic addition increases the deposition rate [49], improves the morphology of the weld bead [51,119], arc process efficiency [119] and the hardfacing process stability [120]. Trembach et al. [49] determined that the introduction of exothermic addition (CuO–Al) of to the core filler had a significant effect on such indicators of the weld bead morphology, microstructure and mechanical properties [87,121–123].

The purpose of this development of an alloy with increased mechanical properties is to compare the phase composition and chemical composition of the phases of calculated data with experimental data for the boron-containing alloy 110Cr4Cu5TiVBAl with a high copper content, and to investigate the mechanical properties of hardfacing alloys.

2. Materials and methods

2.1. Materials and conditions

For testing, templates were made, cut out of S235J2G2 EN10025–2 preliminarily deposited on the plate using flux-cored arc

Table 1
Hardfacing conditions used in flux cored wire arc process.

Travel speed TS, mm·s^{-1}	Contact tip to work distance CTWD, mm	Arc voltage Ua, V	Weld-ing curent I, A	Heat inpute HI, kJ·mm^{-1}	Initial tempera-ture T_0, °C	Prehea-ting Tp, °C	Thermal conductivity λ, J/(s·m·°C)	Cooling time $\Delta t_{8/5}$	Cooling rate CR, °C/s
5.14	40	27.72	369.32	1.494	25	220	42	6.95	43.2

welding. Hardfacing was applied in four layers. Table 1 was shown the used hardfacing conditions used when hardfacing with a self-shielding flux-cored wire electrode with an exothermic addition in the core filler. After that, the samples were subjected to mechanical processing in modes that exclude overheating and tempering of the deposited metal. The chemical composition of the deposited metal is given in Table 2.

2.2. Microstructure observation and mechanical properties measurement

The microstructure of the hardfacing layer was observed by scanning electron microscopy (SEM) using a ZEISS EVO 40XVP (ZEISS Group, Jena, Germany) scanning microscope, with the INCA ENERGY 350 (Oxford Instruments, Abingdon, UK) X-ray microanalysis system, at the Center for Collective Use of Scientific Instruments "Center for ElectronMicroscopy and X-ray Microanalysis" of the Karpenko Physico-Mechanical Institute of the National Academy of Sciences of Ukraine (Lviv, Ukraine).

Depth-sensing indentation found wide application for mechanical properties measurements of modified surface layers [124–128], sintered metal composites [129], iron-rich borides and carboborides [130].

Indentation tests were carried out using multifunctional indentation tester "Micron-gamma" of the National Aviation University (Kyiv, Ukraine) [131,132]. Indentation curve recorded during Berkovich diamond tip penetration into the samples of metal alloy 110Cr4Cu6Si1MnBTi allows to determine the indentation hardness and modulus, the resistance to plastic deformation and other mechanical parameters. The indentation test parameters used in this work are presented in Table 3. Samples were cut from welded plates according to the procedure presented in the work [48].

3. Results and discussions

3.1. Simulated solidification process using Thermo-Calc

Thermo-Calc was used to create phase mass fraction diagrams (so-called "property diagrams") (Fig. 1), which show the evolving phase fractions as a function of decreasing temperature for a specific composition.

Fig. 2 a-i depicts the relationship between the composition ratio of each precipitated phase and temperature in the experimental steel. As shown by the results of chemical composition modeling for the phase M_2B_CB (Fig. 2 h) it will contain the following proportion of the main chemical elements: Fe = 0.4–0.5; Cr = 0.37–0.44; B = 0.09; Mn = 0.03–0.06. Such a composition correspond to the CrFeB-type boride. It should also be noted that, in this case the volume fraction of the $M_7C_3\_D101$ phase continues to grow. Liquid phase is almost disappeared at a temperature about 1200 °C. As a consequence, the M_2B_CB (CrFeB type boride) and $M_7C_3\_D101$ (chromium carbides $Cr_4Fe_3C_3$) phases will precipitate from the solid solution of the FCC_A1#3 phase (γ–Fe phase).

It is interesting to investigate the chemical composition of formed phases for better understanding of the solidification process of the alloy subject to study, as well as the changes in their chemical composition for each phase and their composition change. The change in the content of each element in each phase was calculated depending on the temperature precipitation, as shown in Fig. 3 to clarify the elements and content of each phase. Statistical analysis was carried out for all types of second phase precipitation using Thermo-Calc as shown in Table 4, mainly including maximum mass fraction of the precipitation, the initial temperature of formation, the temperature of complete breakdown, etc.

Continuation of intense precipitation of CrFeB type boride phases and chromium carbides $Cr_4Fe_3C_3$ leads to depletion of the liquid alloy in chromium, as evidenced by Fig. 4 b composition of the liquid phase in the temperature range from 1167 °C to 1152 °C. At that, the mass fraction of manganese (Mn) and iron (Fe) in the liquid alloy increases, while the mass fraction of other chemical elements remains almost unchanged. Further cooling of the liquid melt leads to an increase in the volume fraction of the M2B_CB and M7C3_D101 phases, as well as the separation of an insignificant amount of the M2B_C16 and CEMENTITE phases. However, their proportion is insignificant, so they were not specified in the phase diagram (Fig. 1). In Table 5, the various transformation temperatures of Grade 110Cr4Cu7Ti1VB alloy are presented.

The primary phase precipitating from the liquid phase is the FCC_A1#2 phase. Its deposition begins at a temperature of 1505.5°C (Fig. 1). Analyzing chemical composition of the phase at the primary stage of solidification (Fig. 2 a), we can state that this phase will be titanium carbides (TiC), having a face-centered-cubic (FCC) lattice (Fig. 1). During the formation of the FCC_A1#2 phase, some part of titanium is substituted by chromium after titanium solution depletion starting from the temperature of 1461 °C. As a result, segregated titanium carbides are incrementally enriched by chromium. The volume of this phase gradually increases up to 0.063 vol fraction (6.3 wt%). Initial precipitation of carbides can be explained by the fact that carbon (C) has higher electronegativity than boron (B). Besides it, B promotes the precipitation of carbide [133].

It is thermodynamically possible for the phase FCC_A1#3 (Fig. 1) being austenite (γFe), to precipitate from the liquid solution at temperature of 1365.78 °C. The first portions of γ–Fe precipitated phase, which contains a large amount of dissolved copper (0.054 vol fraction) (Fig. 2 b). The solution contains less chromium (0.034 vol fraction) (Fig. 2 b) and carbon 0.0033 vol fraction. The liquid phase

Table 2
The chemical composition of the deposited metal, mas.% [3].

C	Cr	B	Ti	Cu	V	Mn	Si	Al	N	P	S	Fe
1.1	4.07	0.45	1.5	5.2	0.26	1.8	1.23	0.5	0.046	0.017	0.031	Bal.

Table 3
Indentation test parameters.

Parameter Types	Value
Max load on the indenter	0.5 N
Loading rate	5 mN/s

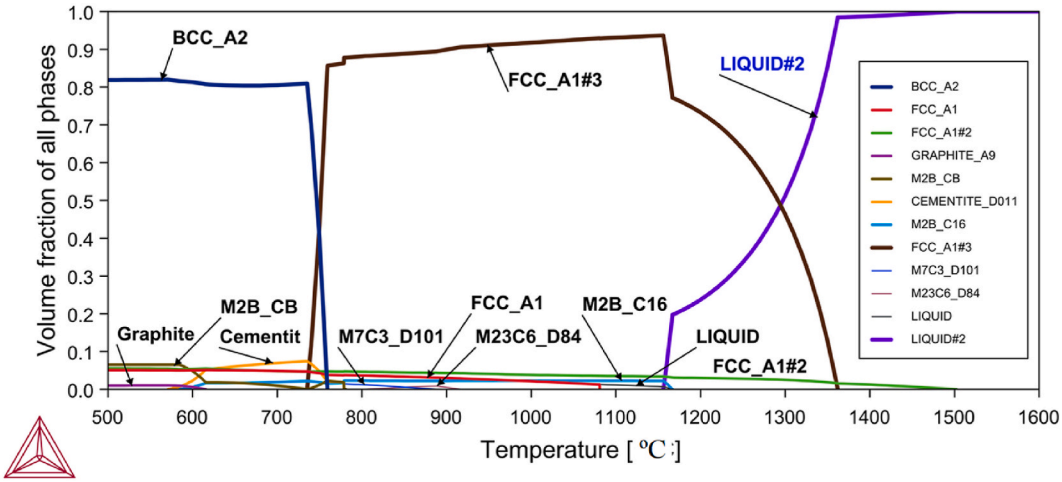

Fig. 1. Phase-quantity graphs (phase fractions) calculated with ThermoCalc for the samples 110Cr4Cu7Ti1VB.

volume fraction begins to decrease quickly, mainly due to the deposition of the γ–Fe phase. Liquid phase is enriched with alloying elements such as chromium, carbon, boron (Fig. 4 a). The mass fraction of copper remains almost unchanged, but the same of titanium decreases. It can be stated that copper is dissolved mostly in the austenite phase. This copper performance during iron alloy solidification is shown in the studies of Ohtsuka [134]. Carbon enrichment of liquid phase and almost constant amount of copper in liquid phase within the temperature range from 1353 °C to 1223 °C is due to the low solubility of carbon, and the limited solubility of copper. Liquid phase enriched with copper is separated from the solution (LIQUID phase composition) at a temperature of 1173.71 °C, in the phase diagram (Fig. 1). This phase will disappear at 1080.57 °C. This phase transitions to a solid phase, being a phase enriched with copper FCC_A1 with a body centered cubic (BCC) structure. Copper appearance as a separate phase is confirmed by the studies of Yi et al. [76]. This precipitation can act as heterogeneous precipitation of pearlite nucleus, resulting in hardenability reducing [76].

Gradual increasing of boron concentration in the remaining solidifying liquid phase (Fig. 4 b), which volume fraction decreased to 0.36 vol from the initial one, leads to precipitation from the liquid M2B_C16 phase of borides. This precipitation occurs when the temperature drops below 1168.55 °C (Fig. 1). According to Fig. 2 d this phase will correspond to hemiboride $(Fe,Cr)_2B$. It gradually transformed in the boride of the M2B_CB phase according to the phase diagram (Fig. 1) at a temperature of 939.45 °C. Hemiboride $(Fe,Cr)_2B$ will be observed in the alloy up to temperature above 603.63 °C. Quick precipitation of remaining part of liquid solution in main form as FCC_A1#3 (Fig. 1) happens. Small amount of cementite and a other phases will also precipitate.

M7C3_D101 phase separates from the solution at temperature below 942.42 °C. Based on the analysis of the M7C3_D101 phase chemical composition we can say that it represents the chromium carbide Cr_7C_3. However, it is completely dissolved in the austenitic matrix at 778.81 °C. At the same time, a small proportion of cementite begins to precipitate from the matrix (779 °C which will slowly turn into graphite), while the remaining volume of the primary austenitic phase transfers mainly into low-alloyed ferrite and a small amount of the hardening phase in the form of M2B_CB (Fig. 1). It should be noted that the precipitated phase M2B_CB will correspond to hemioboride FeCrB, which contains a large amount of chromium (Fig. 2 f and 2 g).

After solidification, boron atoms and other metal atoms diffused into cementite in the pearlite, resulting in the formation of boron-cementite $M_3(B,C)$ (Fig. 2 h).

3.2. CCT diagram and welding cycle

As known, a hardfacing process is characterized by processes nonequilibrium due to a high cooling rate and welding deformations and stresses formation (thermal welding cycle (TWC)). The phase separation under such conditions occurs according to the grain formation and growth mechanism. High overcooling (supersaturation) degrees and long soakings at appropriate temperatures are required to start transformation. Transformations nature depends on the alloy composition, maximum temperatures of heating, depending on speed and deformation parameters of a TWC. The difference of free energies (thermodynamic potentials) is the transformations driving force. Phase transformation kinetics at various degrees of overcooling is shown at Continuously cooling transformation (CCT) diagram [135]. We implemented JMatPro program to predict the phase structure and the chemical composition of the

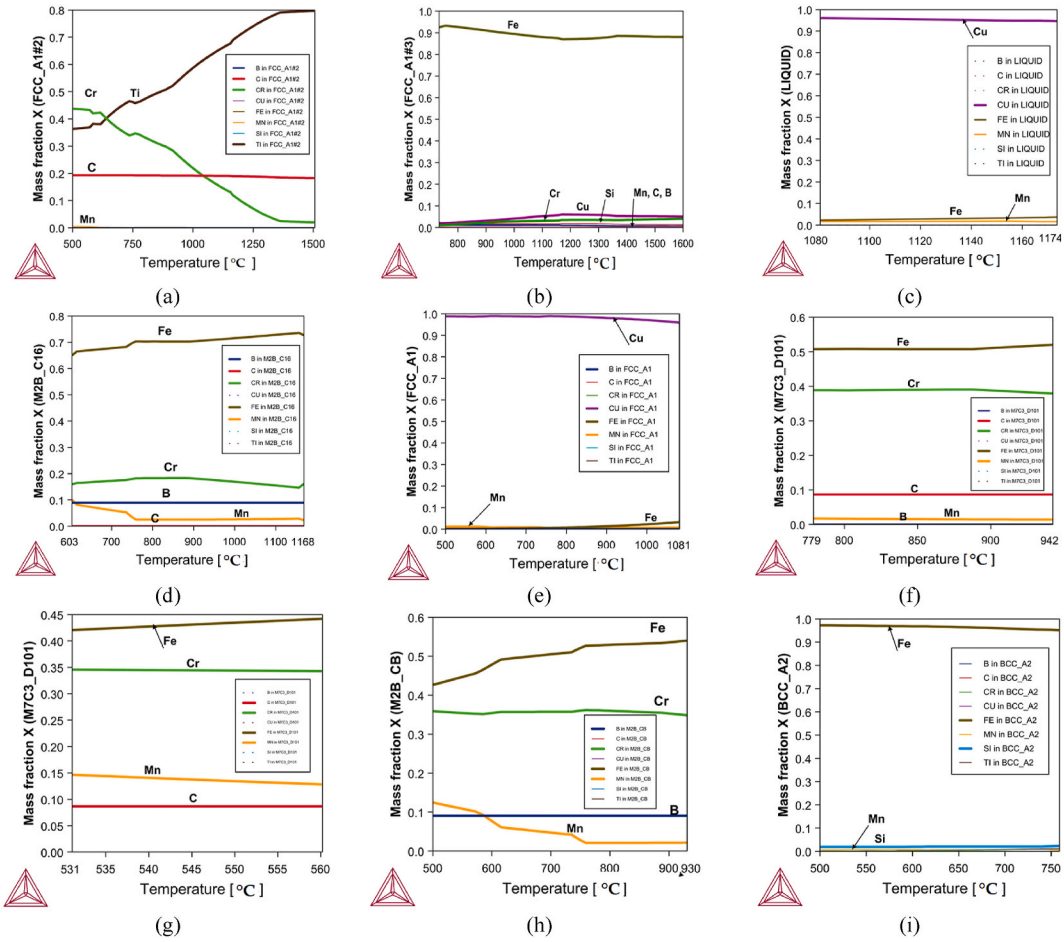

Fig. 2. The relation between the composition ratio of each precipitated phase and temperature in experimental steel: (a)-FCC_A1#2; (b)-FCC_A1#3; (c)-LIQUID; (d)-M2B_C16; (e)-FCC_A1; (f)-M7C3_D101; (g)-M7C3_D101; (h)-M2B_CB; (i)-BCC_A2 of the 110Cr4Cu5Si1MnBTi.

phases forming during the hardfacing process [123].

Continuously cooling transformation (CCT) diagram was received based on the simulation results.

The CCT diagram (Fig. 5) shows the formation of three phase regions (martensite, bainite and pearlite) depending on the selected cooling rate. The critical cooling rate, when we get an exclusively homogeneous microstructure of martensite (+ residual austenite), is calculated to be approximately 30 °C/s. The temperature Mf is not shown on the diagram because the investigated experimental material contains 1.1% C, and as is known, increasing the proportion of C content shifts the temperature of the final Mf to negative temperatures. The Ps temperature at slow cooling rates has an approximate temperature of ~758 °C. For this reason, the authentication temperature should generally have a value of at least 50 °C above this temperature.

Fig. 6 represents the development and proportion of different phases during a cooling rate of 45 °C/s. The solidification of the liquid phase (Liquid) into a solid phase begins at a temperature of 1365 °C. Ferrite is partially transformed from austenite at a temperature of approximately 800 °C. Taking into account the welding technology (preheating temperature 220 ± 15 °C), we expect to have a three-phase matrix containing mainly austenitic (~60 wt%) and martenitic (~30 wt%) phases, as well as not a large part of the ferritic phase (~10 wt%).

3.3. *Elemental distribution (scanning electron microscopy)*

Fig. 7 shows a map of the distribution of alloying elements in the deposited metal, examined using EDS mapping analysis. Fig. 7 a shows a scanning electron microscope (SEM) image, and Fig. 7 b shows a statistical diagram presenting the content of alloying elements.

Analizing an alloying elements distribution (Fig. 7 g, h,i,j) we can notice that the carbon is concentrated in the area of titanium and vanadium and their carbides accumulation ((Ti,V)(C,N)). In addition, a nitrogen is also concentrated in this area.

Iron is concentrate more in the matrix (Fig. 7 c). Its concentration in borides areas is lower $(Fe,Cr)_2(B,C)$. It was revealed that there is almost no iron in carbide titanium formation areas. Manganese has a nature of distribution between the matrix and the changing

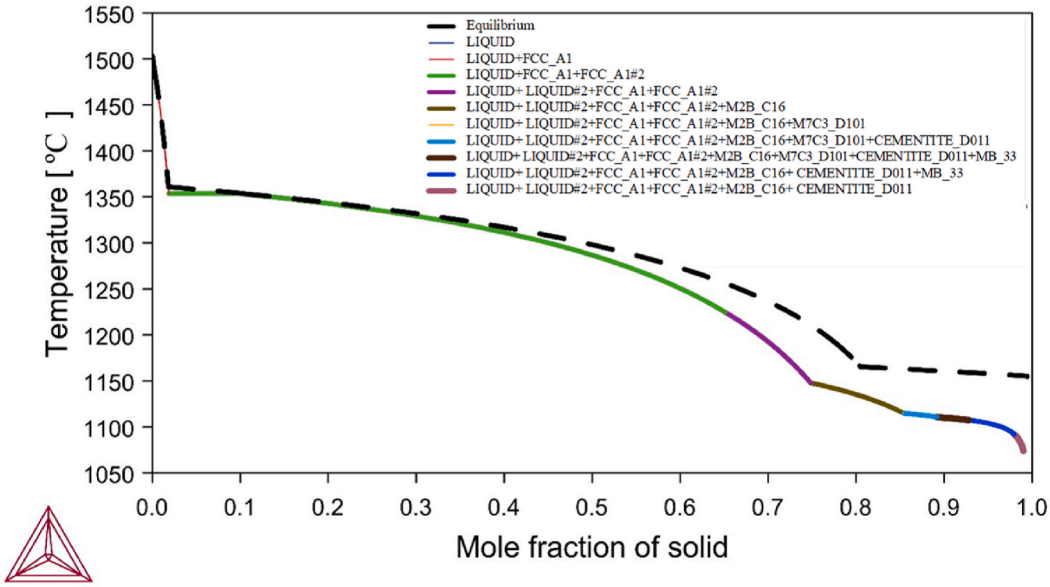

Fig. 3. Scheil solidification diagram of the 110Cr4Cu7Si1MnBTi alloy using by Thermo-Calc analysis.

Table 4
Predicted phases, their chemical formulas and temperatures of existence, modeled with Thermo-Calc.

Parameter	Phase							
	FCC_A1#2	FCC_A1#3	M2B_C16	FCC_A1	M7C3_D101		M2B_CB	BCC_A2
	TiC	γ–Fe (austenite)	Fe_2B	Cu	Cr_7C_3		CrFeB	α-Fe (ferrite)
Chemical formula	TiC	γ–Fe	$Fe_{1.6}Cr_{0.4}B$		$Cr_3Fe_4C_3$	$(Fe_3Cr_{2.5}Mn_{1.5})C_3$	$Fe_{1.25}Cr_{0.75}B$	α-Fe
Phase appearance temperature, °C	1505.48	1365.78	1168.55	1080.72	942.42	560.2	939.45	758.65
Min phase existence temperature in the considered range, °C	500	733.22	603.63	500	778.82	531.1	500	500

phases similar to the iron, but its concentration level was higher in the boride phase then in the matrix (Fig. 7 *l*). This is confirmed by the higher color brightness (Fig. 7 l) in these areas and the EDX analysis results. Chromium is almost absent on the titanium carbide formation areas (Fig. 7 d). The obtained results are similar to those of Zhang et al. [136]. This distribution of alloying elements can be explained by the atomic radii ratio and an external electronic configuration structure, by the ratio of atomic radii and external electronic configuration. In the first place, the propensity for the solutes to form solid solutions involves the crystallographic aspect. To estimate the solubility of the alloying elements, the $(r_0 - r)/r_0$ ratio should be of use, where r-atomic radius of the solvent, r_0-atomic radius of the solutes. Elements in the order of atomic radii increasing can be arranged in the following series (according to Belov–Bokiyu): Fe→Cr→Ni→Cu→Mn→V→Si→Mo→Al→Nb→Ti. Probability of iron atoms replacement in borides by atoms of alloying elements in the solid solution decreases correspondingly. In addition, electronic configuration has influence to the elements solubility and their ability to be valency electron sources or their acceptors.

Due to the fact that the titanium atom has the largest atomic radius in the series, compared to the iron (Fe) atom the probability of iron atoms replacement in borides and in the matrix by titanium atoms is very low. Ti atoms possess negative charges and thus act as electron acceptors. It can explain almost complete absence of titanium in the borides and in the matrix. The obtained results showed that titanium is almost completely contained in its own carbide Ti(C, N) in the studied alloy of Fe–B–C–Cr–Ti. It also can be explained by the significant thermodynamic probability of the titanium carbides formation in calculations made (Fig. 2 a). The ions of such elements as Mn, V, Cr, have p6–shells and form with boron the same valence bonds like the atoms of iron. In addition, manganese atoms partially replace iron atoms in crystal lattices [137]. Solid replacement solutions are formed correspondingly [74].

At the same time, copper, silicon and aluminum are concentrated mainly in the matrix (Fig. 7 e, k, m). Aluminum and silicon are sp-elements, whereas copper atomic configurations tend to the stable d5–states. The higher solubility of Al and Si in the boron-rich Fe–B–C alloys, as compared with Ti, may be attributed to the stronger acceptor abilities of these elements [65]. Copper is not dissolved in hemioboride $Fe_2(B,C)$ and borocementite $Fe_3(B,C)$, but titanium carbide TiC is dissolved only in the matrix. Similar results have been obtained by other researchers [74,96–98]. This solubility of copper is explained by the electronic structure of its atoms. According to Sukhova [74] copper atoms have the following outer electron configuration: d10s2, due to which it cannot accept

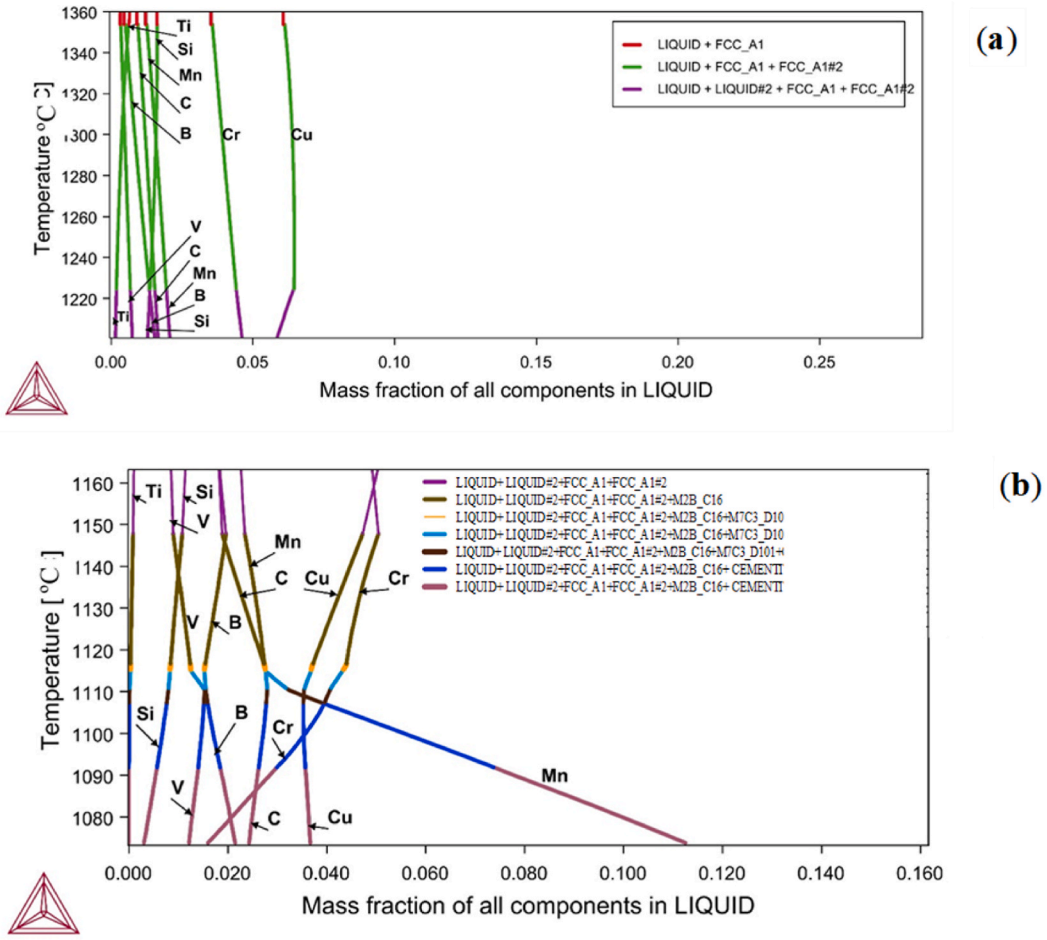

Fig. 4. Element concentration in the liquid phase during solidification estimated with the Scheil–Gulliver approach in the range below: (a)-1200–1360 °C; (b)-1070–1160 °C.

Table 5
Various transformation temperatures of Grade 110Cr4Cu7Ti1VB alloy.

Description of Phase Change	Temperature, °C
α–Fe+CrFeB + TiC + Cu–phase → α–Fe+CrFeB + TiC + Cu–phase + Cr_7C_3	531.1
α–Fe+CrFeB + TiC + Cu–phase + Cr_7C_3 → α–Fe+CrFeB + TiC + Cu–phase	560.2
α–Fe+CrFeB + TiC + Cu–phase → α–Fe+CrFeB + TiC + Cu–phase + Fe_2B	603.63
α–Fe+CrFeB + Fe_2B + TiC + Cu–phase → α–Fe+CrFeB + Fe_2B + TiC + Cu–phase+γ–Fe	603.63
α–Fe+CrFeB + Fe_2B + TiC + Cu–phase → α–Fe+CrFeB + Fe_2B + TiC + Cu-phase+γ–Fe	733.22
α–Fe+γ-Fe+CrFeB + Fe_2B + TiC + Cu–phase → γ–Fe+CrFeB + Fe_2B + TiC + Cu–phase	758.65
γ–Fe+CrFeB + Fe_2B + TiC + Cu–phase → γ–Fe+CrFeB + Fe_2B + TiC + Cu–phase + Cr_7C_3	778.82
γ–Fe+CrFeB + Fe_2B + TiC + Cu–phase + Cr_7C_3 → γ–Fe + Fe_2B + TiC + Cu–phase + Cr_7C_3	939.45
γ–Fe + Fe_2B + TiC + Cu–phase + Cr_7C_3 → γ–Fe + Fe_2B + TiC + Cu–phase	942.42
γ–Fe + Fe_2B + TiC + Cu–phase → γ–Fe + Fe_2B + TiC + Cu–phase + Liquid Cu	1080.57
γ–Fe + Fe_2B + TiC + Cu–phase + Liquid Cu → γ–Fe + Fe_2B + TiC + Liquid Cu	1080.72
γ–Fe + Fe_2B + TiC + Liquid Cu → γ–Fe + Fe_2B + TiC + Liquid Cu + L	1158.8
γ–Fe + Fe_2B + TiC + Liquid Cu → γ–Fe + TiC + Liquid Cu + L	1168.55
γ–Fe + TiC + Liquid Cu + L → γ–Fe + TiC + L	1173.71
γ–Fe + TiC + L → TiC + L	1365.78
TiC + L → L	1505.48

additional electrons, serving only as a source of valence electrons It makes difficult the delivery of the electrons and imposes restrictions on the electron exchange. It means that Cu doesn't react with B [76]. Therefore, the solubility of Cu in carboboride crystals is practically absent.

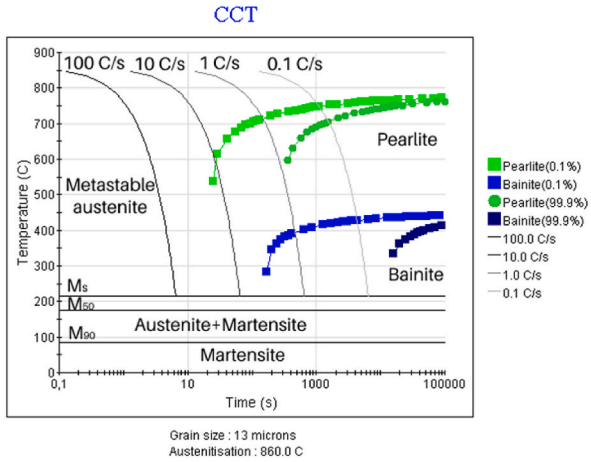

Fig. 5. Continuously cooling transformation (CCT) diagram of the 110Cr4Cu7Si1MnBTi deposited metal.

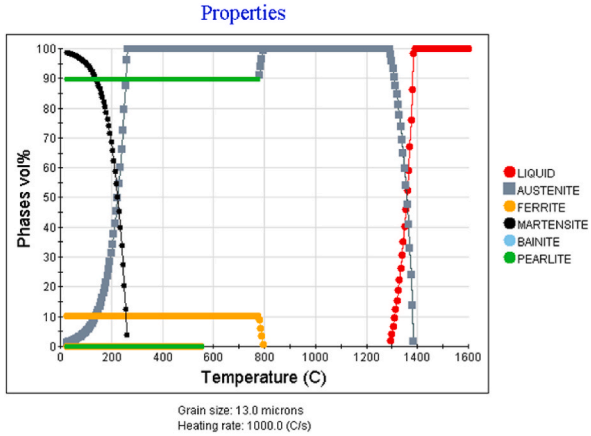

Fig. 6. Influence of the welding cycle (Rate of heating RH = 1000 °C/s, cooling rate CR = 45 °C/s, graine size 13 μm) on the phase composition of the deposited metal during FCAW–S process.

3.4. Microstructure

Fig. 8 a, b shows the microstructure of medium-boron deposited metal with a low content of chromium (4% wt.) and a high content of copper (5% wt. Cu). The microstructure of the hardfacing layer was observed by scanning electron microscopy using a ZEISS EVO 40XVPmicroscope, with the INCA Energy X-ray microanalysis system.

In order to clarify the microstructural evolution of deposited metal, the chemical composition of the above-mentioned points was analyzed by EDS. Energy dispersive X-ray spectrometer INCA ENERGY 350 with microanalytical INCA X-stream processor, Microscope Image Capture System (MICS) and Inca Energy software. The results of the studies were presented in Fig. 9 and Table 6.

Indent with mark 1 represents γ–Fe + Cr_7C_3 eutectic as a matrix. According to the results of the analyzes performed by electronic probe microanalyzer (EPMA), we can conclude that the matrix dissolved almost all copper (Table 6). It confirmed the results of the other researchers studies as the predominant dissolution of copper in austenite [75,96,107]. However, other researchers underline an existence of copper in the matrix in the form of its own ultrafine copper phase [76]. These statements were also confirmed by our thermodynamic calculations. It is necessary to perform additional researches to make a high quality analysis.

Marker 2 corresponds to titanium carbides, in which some part of titanium is replaced by a small amount of vanadium, niobium and chromium (Table 6). Titanium carbides (TiC) are uniformly distributed in the deposited metal in the form of separate parts. It may be noted that we observed a relatively large amount of dissolved iron in titanium carbide. As it was already mentioned, the hardfacing process is characterized by nonequilibrium solidification conditions. It caused an increasing of iron content in TiC. Therefore the ternary (Ti,Fe)C systems were formed. It is also confirmed by Råsander et al. [138].

Investigation performed by EPMA showed that the edged phase in the form of network is hemiboride Fe_2C. The results showed that some of iron atoms will be substituted by chromium atoms, and the compound will correspond to the following chemical formula: $Fe_{1.8}Cr_{0.2}B$ (Table 6). It should be noted that Fe_2B represents an edged phase. Studies of Filonenko and Galdina [139] and Koifman

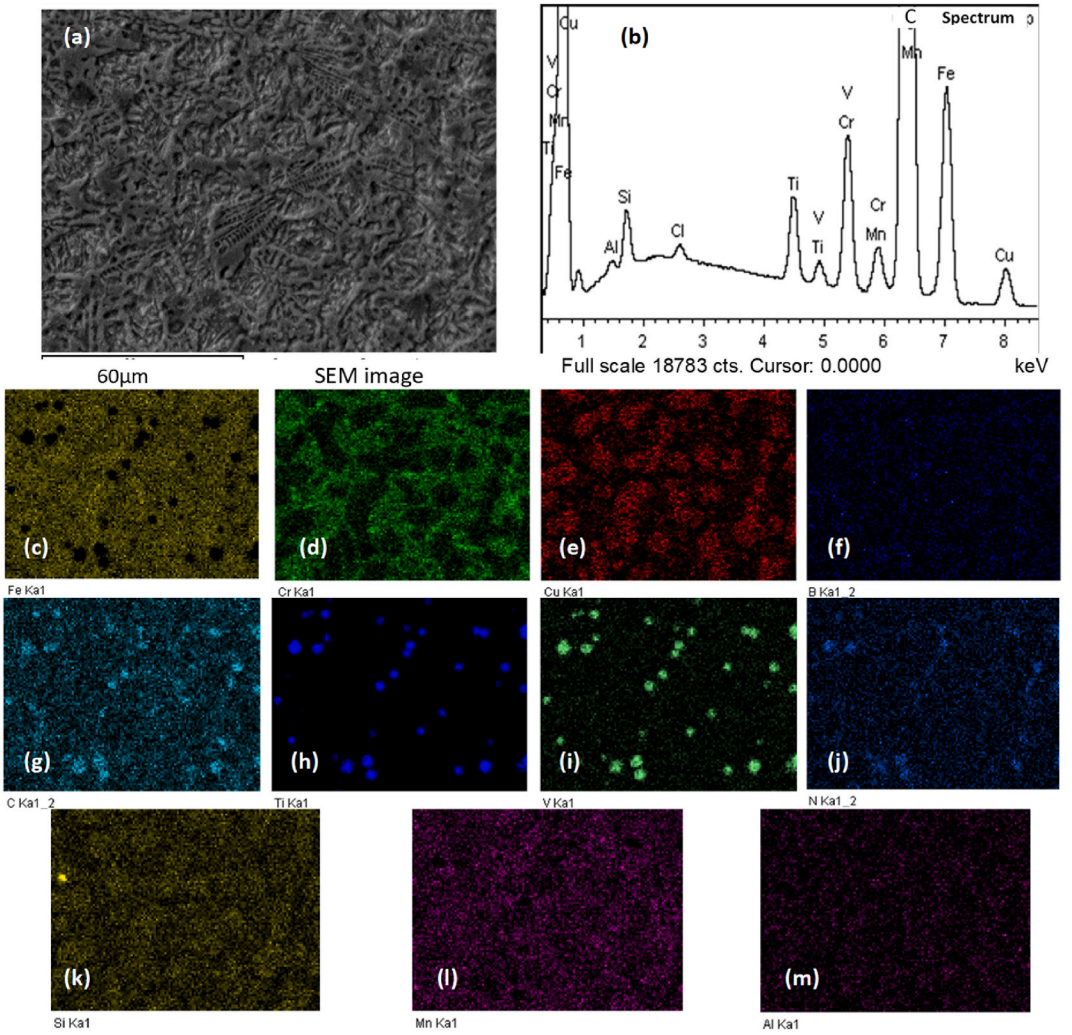

Fig. 7. Diagram of the distribution of elements in the developed alloy 110Cr4Cu7Si1MnBTi: (a)-SEM image; (b)-a statistical diagram for alloying elements content; (c) iron (Fe); (d)-chromium (Cr); (e)-copper (Cu); (f)-boron (B); (g)-carbon (C); (h)-titanium (Ti); (i)-vanadium (V); (j)-nitrogen (N); (k)-silica (Si); (l)-manganese (Mn); (m)-aluminum (Al).

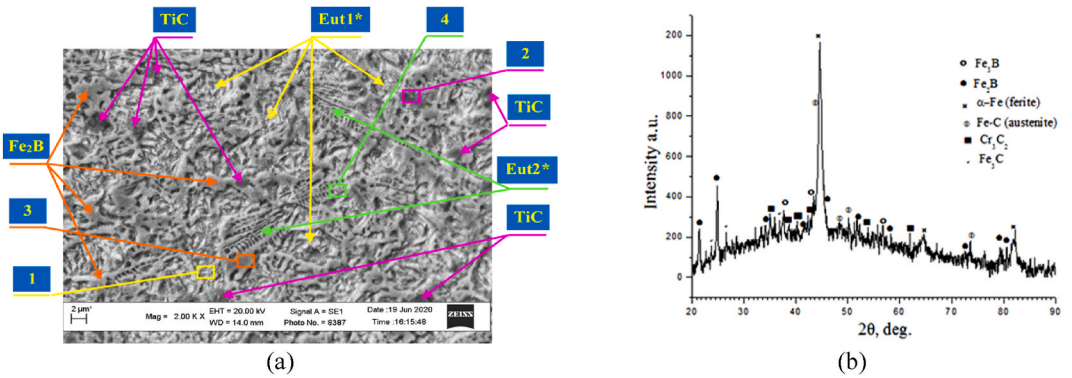

Fig. 8. The images of the microstructures x1000 (a) and XRD pattern (b) [87] of deposited metal in 3 layers hardfacing by FCAW–S-110Cr4Cu5Ti1VB.

Mark 1

Element	Wt. %	at. %
C K	3.04	12.62
Al K	0.41	0.76
Si K	1.45	2.56
Cr K	2.41	2.30
Mn K	0.99	0.90
Fe K	83.18	74.18
Cu L	8.52	6.68
Sum	100.00	

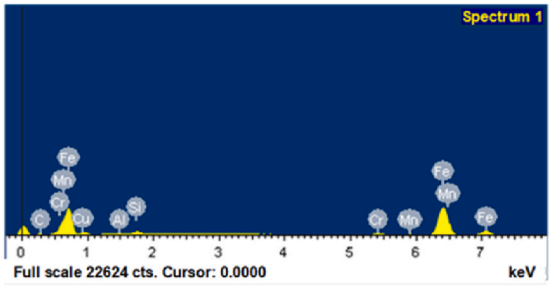

Mark 2

Element	Wt. %	at. %
C K	16.51	45.17
Si K	0.33	0.39
Ti K	61.48	42.19
V K	2.73	1.76
Cr K	1.55	0.98
Fe K	14.29	8.41
Nb L	3.12	1.10
Sum	100.00	

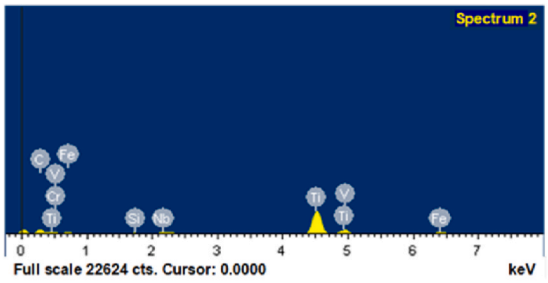

Mark 3

Element	Wt. %	at. %
B K	10.74	35.75
C K	2.67	8.01
Ti K	0.36	0.27
V K	0.38	0.27
Cr K	7.98	5.52
Mn K	1.07	0.70
Fe K	76.79	49.47
Sum	100.00	

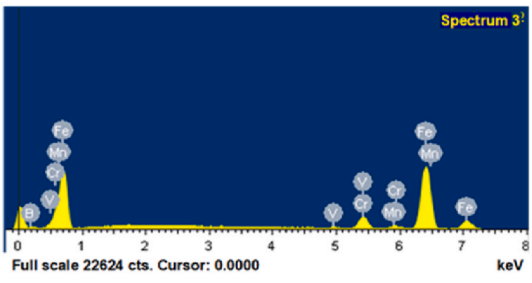

Mark 4

Element	Wt. %	at. %
B K	3.31	13.30
C K	3.00	13.19
Si K	0.38	0.60
Cr K	14.52	12.12
Mn K	2.18	1.72
Fe K	75.96	59.06
Sum	100.00	

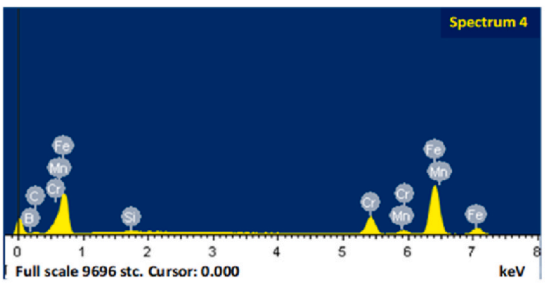

Fig. 9. Chemical composition of the region (phases) of the deposited metal for different markers shown in Fig. 8 according to EDX analysis data and its typical EDX spectra.

Table 6
Compositions of the austenite (γ–Fe), M_2B and $M_{23}(B,C)_6$ measured by using an EDX analysis data.

Phase	Element, at.%								Calculated Formula
	B	C	Fe	Cr	Si	Mn	Ti	Other	
Eutectic γ–Fe + Cr_7C_3	–	3.04	83.18	2.41	1.45	0.99	–	8.52Cu	$Fe_{0.79}Cu_{0.07}Si_{0.02}Mn_{0.01}$ $C_{0.11}$+ +$Cr_{6.5}$(Si, Mn)$_{0.5}C_3$
TiC	–	16.51	14.29	1.55	0.33	3.12(Nb)	61.48	2.73V	$Ti_{0.81}Fe_{0.19}C$
Fe_2B	10.74	2.67	76.79	7.98	–	1.07	0.36	0.38 V	$Fe_{1.8}Cr_{0.2}B$
$Fe_3(B,C)$	3.26	3.0	75.96	14.52	0.38	2.18	–	–	$Fe_{2.5}Cr_{0.5}B_{0.5}C_{0.5}$

et al. [140] showed the possible partial substitution of boron by carbon atoms. They attributed this to the similar cation radii and bonding behavior of B and C. Experiments [139] showed the possibility of boron atoms substitution by carbon atoms in the Fe_2B boride crystal lattice within the range of 0.15–0.4 (wt.%).

Whereas the dendrites are $Fe_3(C)$ with a ferrite phase between dendrites. Borocementite formation can be explained by the fact that some carbon atoms in cementite were replaced by boron atoms. Filonenko [141] confirmed that boron atoms can substitute up to 80% (at.) of carbon atoms in cementite (Fe_3C). It is explained by the lower Gibbs energy of $Fe_3(C,B)$ borocementite formation compared to the Gibbs energy of Fe_3C cementite formation.

Thus, the alloy structure could be a matrix in the form of a γ–Fe+Cu+Cr_7C_3 eutectic, a hemioboride $M_2(B,C)$ lattice with individual large TiC particles, and a ferrite–boron–cementite eutectic α–Fe + $Fe_3(B, C)$. $M_2(B, C)$ was a product of a eutectic reaction that existed as a lattice boron carbide in the microstructure. It should be noted that the hemioboride $Fe_2(B,C)$ phase joints to the titanium carbide (TiC) particles.

3.5. Mechanical properties by first-principles investigations

Due to the grain's small size, indentation points correspond to two phases or eutectics. It is necessary to analyze the data obtained experimentally and the mechanical properties of individual phases obtained theoretically to make a qualitative analysis. It would improve an understanding and analyzing of mechanical properties obtained by common tests. The criteria for mechanical stability of an unstressed crystalline system are determined by elastic constants inequality [142].

The first-principles calculations based on density functional theory (DFT) are performed using the CAmbridge Serial Total Energy Package (CASTEP) code [143]. The generalized gradient approximation (GGA) with the Perdew-Burke-Ernzerhof (PBE) functional [144] is used to predict the exchange-correlation energy, which depends on both the electron density and its gradient at any point within the crystal. The shear modulus, G represents the resistance to plastic deformation, while the bulk modulus, B represents their resistance to fracture. The valence electronic configurations of the elements used in this work are represented as follows: $2s^22p^2$ (C) and $2s^22p^1$ (B), $3d^34s^1$ (Ti), $3d^34s^1$ (Cr), $3d^74s^1$ (Fe) and $3d^{10}4s^1$ (Cu). A list of phases considered in the calculation and their compounds is provided in Table 7 and Table 8. The calculated values of lattice parameters for the investigated phases are presented in Table 9.

In order to use a calculation procedure for mechanical properties, it is necessary to determine the elastic stiffness constants first. These constants characterize the bond strength in a certain direction. Elastic constants (the cubic and tetragonal phases) were calculated depending on the crystal lattice phases structure, according to the method proposed by Mehl et al. [151]. Calculated elastic stiffness constants for studied phases were shown in Tables 10–12.

Once elastic constants have been obtained, the bulk modulus (B) and shear modulus (G) can be determined. For the tetragonal crystal, the Voigt bound of (B_V) and (G_V) in the hexagonal system can be estimated as Eqs. (1) and (2) [154], orthorhombic crystals as Eqs. (3) and (4) [155,156]:

$$B_V = \frac{2\cdot(C_{11}+C_{12})+4\cdot C_{13}+C_{33}}{9} \tag{1}$$

$$G_V = \frac{12\cdot(C_{44}+C_{66})+C_{11}+C_{12}+2\cdot C_{33}-4\cdot C_{13}}{30} \tag{2}$$

$$B_V = \frac{1}{9}\cdot(C_{11}+2\cdot C_{12}+2\cdot C_{13}+C_{22}+2\cdot C_{23}+C_{33}) \tag{3}$$

$$G_V = \frac{1}{15}\cdot(C_{11}-C_{12}-C_{13}+C_{22}-C_{23}+C_{33}+3\cdot C_{44}+3\cdot C_{55}+3\cdot C_{66}) \tag{4}$$

The Reuss bounds of B_R and G_R are for tetragonal structure Eqs. (5) and (6) [154], Orthorhombic Eqs. (7)–(11) [155,157]:

$$B_R = \frac{C_{33}\cdot(C_{11}+C_{12})-2\cdot C_{13}^2}{C_{11}+C_{12}+2\cdot C_{33}-4\cdot C_{33}} \tag{5}$$

Table 7
Chemical compositions of calculated phases.

Phase	Compounds	Alloy composition, wt.%					
		Fe	Cr	Ti	Cu	C	B
γ–Fe (austenite+(C,Cu))	$Fe_{0.79}Cu_{0.08}C_{0.13}$	87.18	–	–	9.78	3.04	–
γ–Fe (austenite + C)	$Fe_{0.87}C_{0.13}$	96.96	–	–	–	3.04	–
Fe_2B	$Fe_{1.75}Cr_{0.25}B_{0.85}C_{0.15}$	80.21	10.67	–	–	1.76	7.36
$Fe_3(B,C)$	$Fe_{2.5}Cr_{0.5}B_{0.5}C_{0.5}$	78.65	15.09	–	–	3.26	3
TiC	$Ti_{0.83}Fe_{0.17}C$	16.92	–	68.6	–	14.48	–

Table 8
Experimental data and the crystal details obtained from the Rietveld refinement.

Parameter	Phase types			
Identification code	γ–Fe (austenite)	(Ti,Fe)C	$(Fe,Cr)_2(B,C)$	$(Fe,Cr)_3(B,C)$
Formula weight	$Fe_{0.79}Cu_{0.08}C_{0.13}$	$Ti_{0.83}Fe_{0.17}C$	$Fe_{1.75}Cr_{0.25}B_{0.85}C_{0.15}$	$Fe_{2.5}Cr_{0.5}B_{0.5}C_{0.5}$
Radiation	FCC	Cubic	Tetragonal	Tetragonal
Crystal system	Fm–3m	Fm–3m	*I4/mcm*	I4

Table 9
Calculated lattice parameters (lattice constants, angle and cell volume) of investigation phases.

Compounds	a, Å	b, Å	c, Å	Unit cell volume *V*′, Å3	Volume per atom Ω, Å3/atom	α	β	γ
$Fe_{0.79}Cu_{0.08}C_{0.13}$ (austenite)	2.78	2.54	2.87	542.95	10.05	81.63	88.86	90.44
$Fe_{0.87}C_{0.13}$ (austenite)	2.84	2.47	2.77	524.23	9.71	89.99	90.01	90.0
γ–Fe(C)[a]	a = b = c = 0.357[a]			–	–	–	–	–
$Ti_{0.83}Fe_{0.17}C$	a = b = c = 4.266			621.09	9.70	90.02	89.97	89.97
TiC[b]	a = b = c = 4.332[b]			–	–	–	–	–
$Fe_{1.75}Cr_{0.25}B_{0.85}C_{0.15}$	a = b = 4.93		4.18	203.78	8.49	90.07	90.03	88.68
$Fe_{1.75}Cr_{0.25}B$[c]	a = b = 5.068[c]		4.199[c]	107.844[c]	–	–	–	–
$Fe_{1.75}Cr_{0.25}B$[d]	5.032[d]	5.031[d]	4.177[d]	105.724[d]	–	–	–	–
Fe_2B[c,e]	a = b = 5.052[c,e]		4.232[c,e]	108.012[c,e]	–	–	–	–
$Fe_{2.5}Cr_{0.5}B_{0.5}C_{0.5}$	8.57	8.04	4.16	286.53	8.95	90	90	89.99
Fe_3C[f]	5.058[f]	6.703[f]	4.506[f]	152.77[f]	–	–	–	–
Fe_3B[g]	5.336[g]	6.608[g]	4.354[g]	153.56[g]	–	–	–	–

[a] Ref. [145].
[b] Ref. [146].
[c] Ref. [67].
[d] Ref. [147].
[e] Ref. [148].
[f] Ref. [149].
[g] Ref. [150].

Table 10
The calculated elastic stiffness constants (C_{11}, C_{22}, C_{33}, C_{44}, C_{55}, C_{66}, C_{12}, C_{13}, C_{14}, C_{15}, C_{16}) of matrix compounds.

Compounds	Phase	Calculated elastic stiffness constants *Cij*, GPa										
		C_{11}	C_{22}	C_{33}	C_{44}	C_{55}	C_{66}	C_{12}	C_{13}	C_{14}	C_{15}	C_{16}
$Fe_{0.78}Cu_{0.07}C_{0.13}Cr_{0.02}$	Triclinic	281	311	304	83	49	109	198	184	0.055	0.47	7.60
$Fe_{0.87}C_{0.13}$	Ortho-rhombic	348	418	340	80	−39	118	246	262	−2.0	2.0	0.025
γ-Fe (C) [a]	Octahedral	389	–	–	60	–	–	145	–	–	–	–

[a] Ref. [152].

Table 11
The calculated elastic stiffness constants (C_{23}, C_{24}, C_{25}, C_{26}, C_{34}, C_{35}, C_{36}, C_{45}, C_{46}, C_{56}) of matrix compounds.

Compounds	Phase	Calculated elastic stiffness constants *Cij*, GPa									
		C_{23}	C_{24}	C_{25}	C_{26}	C_{34}	C_{35}	C_{36}	C_{45}	C_{46}	C_{56}
$Fe_{0.78}Cu_{0.07}C_{0.13}Cr_{0.02}$	Triclinic	185	37	23	2.34	−0.568	−6.69	1.42	−17.61	6.67	15
$Fe_{0.87}C_{0.13}$	Ortho-rhombic	247	−3.11	10	0.02	1.25	6.25	−0.03	3.47	0.40	0.78

$$G_R = \frac{5 \cdot (C_{11} + C_{12}) \cdot C_{44}}{4 \cdot C_{44} + 3 \cdot (C_{11} - C_{12})} \tag{6}$$

$$B_R = \chi \cdot [C_{11} \cdot (C_{22} + C_{33}\text{-}2 \cdot C_{23}) + C_{22} \cdot (C_{33}\text{-}2 \cdot C_{13})\text{-}2 \cdot C_{33} \cdot C_{12} + C_{12} \cdot (2 \cdot C_{23}\text{-}C_{12}) + C_{13} \cdot (2 \cdot C_{22}\text{-}C_{13}) + C_{23} \cdot (2 \cdot C_{13} + C_{23})]^{-1} \tag{7}$$

$$G_R = 15 \cdot \{4 \cdot [C_{11} \cdot (C_{22} + C_{33} + C_{23}) + C_{22} \cdot (C_{33} + C_{13} + C_{33} \cdot C_{12} - C_{12} \cdot (C_{23} + C_{12}) + C_{13} \cdot (C_{12} + C_{13}) - C_{23} \cdot (C_{13} + C_{23})]/\chi + 3 \cdot (C_{44}^{-1} + C_{55}^{-1} + C_{66}^{-1})\}^{-1} \tag{8}$$

$$B_R = \frac{(C_{11} + C_{12}) \cdot C_{33} - 2 \cdot C_{13}^2}{C_{11} + C_{12} + 2 \cdot C_{33} - 4 \cdot C_{13}} \tag{9}$$

Table 12
The calculated elastic stiffness constants of investigation hard phases along with other available values.

Compounds	Phase	Calculated elastic stiffness constants *Cij*, GPa								
		C_{11}	C_{12}	C_{13}	C_{23}	C_{22}	C_{33}	C_{44}	C_{55}	C_{66}
$Ti_{0.83}Fe_{0.17}C$	Cubic	513	130	–	131	–	–	156	–	–
TiC[a]	Cubic	517	117	–	–	–	–	174	–	–
TiC[b]	Cubic	519	115	–	–	–	–	183	–	–
$Fe_{1.75}Cr_{0.25}B_{0.85}C_{0.15}$	Tetragonal	506	252	245	248	499	423	133	129	121
$Fe_{1.75}Cr_{0.25}B$[c]	Tetragonal	436.2	171.7	143.4	143.4	436.2	370.4	161.3	161.3	151.9
Fe_2B[c]	Tetragonal	413.4	153.4	128.5	128.5	413.4	387.7	148.0	148.0	156.2
$Fe_{2.5}Cr_{0.5}B_{0.5}C_{0.5}$	Tetragonal (I4)	451	283	224	235	489	522	134	117	136
Fe_3C[d]	Tetragonal (I4)	388	156	164c	162	345	322c	15	134c	134c
Fe_3B[e]	Tetragonal (I4)	281.7	337.5	165.3	182.2	337.5	354	130.2	118.7	175.6

[a] Ref. [153].
[b] Ref. [146].
[c] Ref. [148].
[d] Ref. [146].
[e] Ref. [150].

$$G_R = \frac{5}{2} \cdot \left\{ \frac{\left[(C_{11} + C_{12}) \cdot C_{33} - 2 \cdot C_{12}^2\right] \cdot C_{44} \cdot C_{66}}{3 \cdot B_V \cdot C_{44} \cdot C_{66} \cdot \left[(C_{11} + C_{12}) \cdot C_{33} - 2 \cdot C_{12}^2\right] \cdot (C_{44} + C_{66})} \right\} \tag{10}$$

with:

$$\chi = C_{13} \cdot (C_{12} \cdot C_{23} + C_{13} C_{22}) + C_{23} \cdot (C_{12} \cdot C_{13} - C_{23} C_{11}) + C_{33} \cdot \left(C_{11} \cdot C_{22} - C_{12}^2\right) \tag{11}$$

At the second stage, we defined the following mechanical properties which are related to the elastic constants: bulk modulus (B_H) and shear modulus (G_H) (using the Voigt–Reuss–Hill (*VRH*) method). Then the Young's modulus (Y) and Poisson's ratio (ν) can also be calculated from the B and G values. The following equations were used to determine the shown mechanical properties Eq. (12)–(16) [122,124,158]:

$$B_H = \frac{B_V + B_R}{2} \tag{12}$$

$$G_H = \frac{G_V + G_R}{2} \tag{13}$$

$$Y = \frac{9 \cdot B \cdot G}{3 \cdot B + G} \tag{14}$$

$$\nu = \frac{3 \cdot B - 2 \cdot G}{2 \cdot (3 \cdot B + G)} \tag{15}$$

The formula for calculated hardness theoretically is as follow:

$$(H_V)_{Tian} = 0.92 \cdot \left(G \Big/ B\right)^2 \cdot G^{0.708} \tag{16}$$

Table 13 shows the results of mechanical property calculations performed using the CASTEP code.

It is important to understand the nature of the bonds and brittle/ductile behaviour to perform a high-quality analysis of the physical-mechanical powers of separate phases. To cover these issues, it is also acceptable to use in the materials science practice, except such mechanical properties as Poisson's ratio (v), Pugh's ratio (G/B) and Cauchy pressure (p_C). The Pugh's ratio, G/B, is a widely used parameter which is associated with brittle/ductile nature of a material [159]. The critical value which separates ductile and brittle materials is around 0.57; i.e. [158], if $G/B > 0.571$, the material behaves in a brittle manner; otherwise the material behaves in a ductile manner [159]. However, the determination of the material behavior should be considered taking into account the Poisson's ratio (ν) [160].

So, materials in which the value of v is 0.33 for ductile/metallic materials. In contrast, for brittle/covalent materials, the v is 0.1, and thus a larger v value states better ductility. Compounds with a value of Poisson's ratio less than $\nu < 0.33$ originate from the more aimed covalent bond as shown in Table 13. It could significantly prevent the generation and movement of dislocations during plastic deformation. As a result, hardness is increased and plasticity is reduced. Cauchy pressure is another indicator characterizing the nature of connections in a bond, which can be used to predict the types of bonds in a solid body.

According to Eberhart and Jones [155], the value of Cauchy pressure (p_C) relative to the zero point reflects the nature of a bond at atomic level. So, it determines the prevailing type of bond. The sign of Cauchy pressure with a dominant covalent bond is negative ($p_C < 0$), and for compounds with a dominant ionic bond or solid solutions with a dominant metallic bond is positive ($p_C > 0$) [161,162]. In

Table 13
The calculated bulk modulus (B), Young (Y) and Shear modulus (G), Pugh's ratio (B/G), Poisson's ratio (v), Cauchy pressure (p_C), Vickers hardness, HV ((all are in GPa unit) for all phases.

Compounds	*B*, GPa	*G*, GPa	*Y*, GPa	Pugh's ratio		*υ*	Cauchy pressure		$Hv^{(Tian)}$, GPa
				k=*G*/*B*	failure mode		p_C	Dominant type of bond	
$Fe_{0.79}Cu_{0.08}C_{0.13}$	224	60	184	0.27	ductile	0.38	115	metallic	3.73
$Fe_{0.87}C_{0.13}$	290	102	274	0.35	ductile	0.34	166	metallic	7.41
γ–Fe(C)[a]	226	80	310	0.35	ductile	0.34	85	metallic	6.29
$Ti_{0.83}Fe_{0.17}C$	258	169	416	0.65	brittle	0.23	−26	covalent	21.50
TiC[b]	251	184	444	0,73	brittle	0.205	−57	covalent	–
TiC[c]	249	190	454	0.76	brittle	0.196	−68	covalent	25.94
$Fe_{1.75}Cr_{0.25}B_{0.85}C_{0.15}$	323	121	322	0.37	ductile	0.33	123	ionic	8.96
$Fe_{1.75}Cr_{0.25}B$[d]	238.63	146.35	364.5	0.61	brittle	0.245	10,4	ionic	18.01
Fe_2B[d]	225.8	143.70	355.7	0.64	brittle	0.237	5.4	ionic	18.54
$Fe_{2.5}Cr_{0.5}B_{0.5}C_{0.5}$	327	122	326	0.37	ductile	0.334	166	ionic	8.96
Fe_3C[e]	224	72	194	0.32	ductile	0.36	22	ionic	5.2
Fe_3B[f]	210	112	285.3	0.53	ductile	0.27	218	ionic	12.7

[a] Ref. [152].
[b] Ref. [153].
[c] Ref. [146].
[d] Ref. [148].
[e] Ref. [149].
[f] Ref. [150].

addition, Cauchy pressure gives negative values for brittle solids, and positive values for ductile metals. The smaller the p_C value is, the greater the brittleness of the compound or solution is, and vice versa. For cubic phases, the Cauchy pressure is calculated according to the following formula $p_c=C_{12}–C_{44}$, while for hexagonal structures $C_{44}=C_{55}$ the formula has the following form $p_c=C_{12}–C_{55}$. Poisson's ratio is another important parameter for understanding of the materials ductile or brittle behavior based on the bonds properties. Higher Poisson's ratio usually shows higher tendency for metallic bonds. It can mean higher strength [163]. Namely, $\nu \geq 0.33$ value means ductile materials, while $\nu \leq 0.1$ value means covalent (brittle) materials. However, the larger ν value is, the better the material plasticity is [160].

We will begin the obtained data analyzing from the matrix, being an important component of wear-resistant alloys. The analysis showed that the austenitic phase enriched with a significant amount of copper ($Fe_{0.79}Cu_{0.08}C_{0.13}$) could have the hardness lower compared to the austenitic phase without copper ($Fe_{0.87}C_{0.13}$). However, we can conclude that the dissolution of copper in austenite phase caused a significant weakening of the shear modulus (*G*). A decrease of shear modulus (*G*) values is an indicator of a smaller bond between atoms [164]. According to the obtained results (Table 13), during comparison of the austenitic phase and the austenitic phase doped with copper we noticed a decrease in shear modulus, comprising almost 1.7 times (60 GPa compared to 102 GPa). As known, the indicator shows the material ability to resist the shear deformation, thus the plastic properties should be improved. According to Eq. (15) it had a significant effect to the Poisson's ratio (*v*). The lower Poisson's coefficient derives from more directional covalent bond. However, the metallic bond remained dominant. Pugh's ratio (*G*/*B*) values indicated (see Table 13) to the plasticity improvement (0.27 compared to 0.35 at a limit value 0.57). Metal bond was also decreased. Cauchy pressure parameter also confirmed it. Moreover, dissolution of a great part of copper led to a decrease of the Young modulus (*Y*) almost to ~1.5 times. It is necessary to specify that despite a significant improvement in ductility, there was a significant hardness reducing (from 7.41 GPa to 3.73 GPa at a high copper content). Probably it was caused by deterioration of the bonds between atoms. It should be noted that according to Table 9, the austenitic phase enriched with copper had an increased lattice parameters in two directions (b = 2.54 Å, c = 2.87 Å con.) and smaller dimensions for one direction (a = 2.78 Å con. a = 2.78 Å). The lattice size increasing in two directions can be explained by the larger sizes of copper atoms compared to implicated iron atoms [74], leading to FCC lattice distortion and interplane distance [165] increasing.

The second phase in the deposited sample structure was hemioboride Fe_2B ($Fe_{1.75}Cr_{0.25}B_{0.85}C_{0.15}$). This phase is important because it forms a lattice in the deposited metal structure and makes a shield protecting an alloy from abrasive wear. Therefore, its properties are also important. Carboboride Fe_2B($Fe_{1.75}Cr_{0.25}B_{0.85}C_{0.15}$) has two specific features. In the first place, iron (Fe) atoms are partially implicated with chromium (Cr) atoms. In the second place, boron atoms (B) are partially displaced by carbon atoms (C). This nature of the hardening phase affects to its final mechanical properties, caused by the difference in the atomic radius and the structure of the external electronic configuration. Arrangement of boron atoms in Fe_2(B, C) carboride lattice can be divided into two sublattices. The first sublattice presents the arrangement of boron atoms, having eight the most close iron atoms c = 4.18 Å (Table 9). In the second sublattice atoms are located at a distance of 4.93 Å from each other (Table 9). It should be noted that with the partial replacement of boron atoms by carbon atoms, the density is decreased (compared to simple hemioboride Fe_2B and chromium-containing hemioboride $Fe_{1.75}Cr_{0.25}B$. According to the studies results shown in Table 13, we observe a significant increase in bulk modulus (*B*) and a significant decrease in the shear modulus (*G*) and the young modulus (*Y*) for carboride phases $Fe_{1.75}Cr_{0.25}B_{0.85}C_{0.15}$, compared to hemioboride Fe_2B and partially displacement with chromium $Fe_{1.75}Cr_{0.25}B$. The partial substitution of boron for carbon changed the character of the hemioboride failure mode from brittle to ductile. It is swown by Pugh's ratio, being k = 0.37 for $Fe_{1.75}Cr_{0.25}B_{0.85}C_{0.15}$, compared to k = 0.61 for $Fe_{1.75}Cr_{0.25}B$. Such plasticity increasing can be explained by a significant grow of the ion bond fraction. It's

evidenced by an increase of the carboboride Cauchy pressure index from $p_C = 10$ to $p_C = 123$. However, a significant increase of ionic bonds proportion and the covalent bond decrease led to the microhardness significant loss. Microhardness value decreased significantly from $HV = 18.016$ GPa to $HV = 8.96$ GPa compared to Fe_2B. This level of microhardness remains enough for effective resistance to abrasive wear. In addition, coefficient value which equals to the critical value of 0.33 shows a significant improvement in the plastic flexible nature of this phase.

The results of our studies showed that the carbide phase is the only brittle phase in the deposited metal structure (with the exception of non-metallic NMI inclusions). As already shown, titanium carbides in our alloy contain a significant amount of iron in their composition. The simulation results obtained by us using density functional theory (DFT) showed a positive effect on the plasticity of titanium carbide when partially replacing titanium atoms with iron atoms (Table 13). It can be explained by a decrease in the clear bond between titanium and carbon atoms in titanium carbide [164], as evidenced by the shear modulus weakening (G ($Ti_{0.83}Fe_{0.17}C$) = 169 GPa compared to pure titanium carbide G(TC) = 190 GPa), and lower values of Pugh's ratio (k($Ti_{0.83}Fe_{0.17}C$)= 0.65 compared to k(TC)=0.76 for pure titanium carbide). Availability of TM impurities significantly affects the stability and mobility of C atoms near TM [138]. Alloying reduces metal-carbon covalent bonds, which predominate in (Ti,M)C. Substitution of Ti by a TM atom with a large number of valence electrons leads to submission of loosening states, which increases the total energy of the system compared to the pure TiC [138]. This leads to chemical bond strength weakening and improves ductility. It is also confirmed by Li et al. [166]. It should be noted that the dominant type of bond for titanium carbide is the covalent bond. It was confirmed by Cauchy pressure substractive values. However, Cauchy pressure is twice higher in the case of partial replacement of titanium atoms by iron atoms in titanium carbides. It is also a confirmation of the plastic properties improvement. A slight decrease in microhardness was observed (from $HV^{(Tian)} = 25.94$ GPa to $HV^{(Tian)} = 21.5$ GPa).

Investigations have shown that the structure contained borcementite $Fe_{2.5}Cr_{0.5}B_{0.5}C_{0.5}$ in which the carbon atoms were partially displaced by boron atoms. Some iron atoms were partially displaced by chromium atoms. The analysis showed that the received borcementite phase had a significantly higher elastic moduli value compared to cementite [146] and exceeded iron boride Fe_3B [150]. It should be noted (Table 13) that shear modulus (G) for borcementite Fe_3(C, B) was significantly greater than the values for cementite Fe_3C, indicating greater bonds between atoms. The bond energy between iron and boron atoms was higher than between iron and carbon atoms. The positive effect of chromium additives can be explained by reducing the B–B bond length to increase bond strength. Pugh's ratio value for borcementite Fe_3(C,B) showed its ductile fracture mode compared to Fe_3B. It means better crack resistance. However, a change of the poisson's ratio ν=0.27 $\leq$ 0.33 for Fe_3B, showed the fracture change nature. For Fe_3(C,B) v = 0,37 $\geq$ 0,33 it indicates the fracture ductile nature. It can be explained by a decrease in an ion bond proportion in the compound, as evidenced by a decrease in Cauchy pressure parameter from k=218 for Fe_3B to k=116 for Fe_3(C,B). Ionicity should always be avoided, as it can have influence to the occurrence of cracks and materials destruction [167]. The phases according to microhardness increasing can be arranged in the following order $Fe_3C > Fe_{2.5}Cr_{0.5}B_{0.5}C_{0.5} > Fe_3B$ (HV=5.2 GPa, $HV = 8.96$ GPa, $HV = 12.7$ GPa according to Table 13). The hardness value can be correlated with the degree of dominant bond according to the values of Cauchy pressure (degree of ion bond Table 13).

3.6. Mechanical properties and indent morphology

Mechanical properties evaluation is one of the most important aspect in developing process of new wear-resistant materials as well as modification of existing ones [168–172]. Wear loss is the result of a complex tribological system reaction which depends not only on contacting materials properties (hardness, strength, plasticity, etc.) but also on the working or testing conditions [173]. Archard proposed the wear model for the sliding adhesive contact in which worn volume is inversely proportional to softer material hardness [174]. However, a significant number of publications have showed many contradictions in abrasive wear resistance and hardness correlation for materials with practically the same hardness but different microstructure.

Ductility index (H/E) [175], plastic deformation index (H^3/E^2) [176], abrasion damage tolerance index $1/(E^2 \cdot H)$ [177] found wide application for materials behavior prediction under abrasive wear on the basis of their mechanical properties. A greater value of H/E indicates a higher load-bearing capacity, so material can effectively withstand higher loads within its elastic limit [178]. The ductility index (H/E) could characterize dissipated energy during damaging process which could be related to the volume of material removed by a single particle impact and thus to the rate of erosion [179]. The ratio H^3/E^2 characterizes the material's ability to withstand plastic deformation during contact and crack resistance, higher value of the parameter indicates higher crack resistance (fracture toughness) [180]. The abrasion damage tolerance index $1/(E^2 \cdot H)$ [177] for determining the resistance of materials to abrasive wear has also become established.

The ten measurements were made with indentation load 50 mN and step 50 μm between indents to eliminate influence of material plastic deformation. Depth-sensing indentation technique allows to determine instrumented hardness (H_{IT}) and elastic modulus (E_{IT}) for each measurement point during single experiment to analyze influence of individual phases, interphase boundaries and multiphase regions on mechanical properties. Moreover, SEM images of the residual indentation impressions formed after indentation tests using Bercovich indenter (Fig. 10 a) were analyzed to identify different phases and phase boundaries. Recorded indentation diagrams are presented in Fig. 10 b. Table 14 shows the data of micro-indentation tests and the values of some indicators.

Indentation results corrected according to procedure reported in Ref. [122] are presented in Table 12 and the SEM images of the indents are shown in Fig. 11. Analysis of obtained experimental results showed that we can subdivide indentation results into 3 groups depending on the phases which were involved in contact with a diamond Bercovich indenter.

Group 1 corresponds to the deposited metal with titanium carbides and eutectic γ–Fe + Cu + Cr_7C_3 and have high hardness and the highest hardness correspond to indents with titanium carbide (Fig. 11 b, h, i). Formed indentation impressions under applied loads are

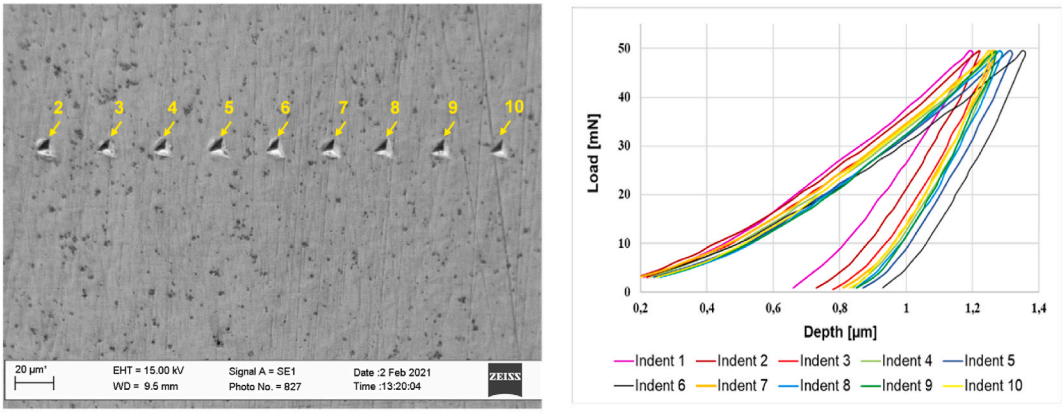

Fig. 10. SEM images of the residual nanoindentation impressions (a) and graph the load vs. depth (P–h) for 10 point (Indent 1–10) (b).

Table 14
Mechanical properties of the investigated 110Cr4Cu7Ti1VB alloy.

Indent	H_{IT}, GPa	E_{IT}, GPa	Ductility index H_{IT}/E_{IT}	Plastic deformation index ($H^3_{IT}/E^2_{IT})\cdot10^{-3}$, MPa	Index of tolerance to abrasion damage ($1/(E^2\cdot H))\cdot10^{-6}$, MPa^{-3}	Phase
1	8.713	283.6	0.031	8.22	1.427	[a]Eut1 + TiC + [b]Eut2
2	9.320	199.2	0.047	20.40	2.704	TiC + [a]Eut1
3	8.252	206.4	0.040	13.19	2.845	Fe_2B + TiC
4	7.773	197.6	0.039	12.03	3.295	Fe_2B+[a]Eut1
5	7.704	204.0	0.038	10.99	3.119	[b]Eut2+ TiC + Fe_2B
6	7.188	202.7	0.035	9.04	3.386	[b]Eut2
7	7.848	199.6	0.039	12.13	3.198	Fe_2B + TiC
8	9.017	210.1	0.043	16.61	2.512	[a]Eut1+ TiC
9	10.057	239.2	0.042	17.78	1.738	TiC + [a]Eut1

[a] Eut1-eutectic γ–Fe + Cu + Cr_7C_3.
[b] Eut2-eutectic α–Fe + Fe_3(B,C).

large than individual phases and we measure integral hardness values, so obtained hardness had predictably lower values compared to the calculated for individual phases. Simultaneously, on the SEM images of the formed indents plastic deformation along the boundaries of the eutectic γ–Fe + Cu + Cr_7C_3 can be clearly seen and indicates high plastic properties. This is also confirmed by the high values of the plastic deformation index (H^3/E^2) obtained for these indents. For group 1 value of H^3/E^2 are $20.4\cdot10^{-3}$ MPa, $16.61\cdot10^{-3}$ MPa and $17.78\cdot10^{-3}$ MPa (Table 14 for indent 2, 8, 9). In addition, mentioned above areas will have higher elastic properties, compared to other areas of the deposited metal (from H/E = 0.47–0.42). It should be noted that the values of abrasion damage tolerance index $1/(E^2\cdot H)$ for such areas showed the lowest values. In this way, areas of deposited metal with titanium carbides showed lower resistance to abrasive wear despite the high integral hardness (Fig. 11 i). It could be explained by a tendency to brittle fracture during interaction with abrasive particles. This is consistent with the Sun et al. [181] results, in which the negative effect of large titanium carbide (TiC) particles was associated with cracking due to increased stress concentration attributed to the accumulation of additional points and one-dimensional (dislocations) defects [182–184] at the boundary of the TiC matrix [181].

We can outline group 2 of indents 3, 4, 7 (see Fig. 11 c, d, g) which characterized by the presents of hemioboride Fe_2B and a small amount of the second phase TiC or eutectica γ–Fe + Cu + Cr_7C_3. Indentation hardness (H_{IT}) of the second group is in the range from 7.77 GPa to 8.253 GPa (Table 14), and it had low values of the indentation modulus E_{IT} = 199.6–206.4 MPa. These arears of deposited metal had relatively high values of ductility index H/E ~ 0.04 and plastic deformation index H^3/E^2=(12.13–13.19)·10^{-3} MPa.

Group 3 indent 1, 5 and 6 (Fig. 11 a, e, f) included areas of deposited metal with eutectic α–Fe + Fe_3(B,C) according to the EDS results. Group 3 characterized by practically similar mechanical properties as in group 2, where the main phase is hemiboride Fe_2B. For the 3 group indentation hardness (H_{IT}) and indentation modulus (E_{IT}) is in the range from 7.188 GPa to 7.04 GPa and 202.7–204 MPa respectively (Table 14 for indent 5, 6). For group 3 values of H^3/E^2 are (9–11)·10^{-3} MPa, H/E are 0.35–0.38), and the values of abrasion damage tolerance index $1/(E^2\cdot H)$ 3.119–3.386 ·10^{-6} MPa^{-3} (Table 14). The experimental data obtained for this group agree with the calculated values of the mechanical properties for these phases. The difference in mechanical properties can be explained by the variable mechanical properties of the matrix phases. Thus, for group 2, the matrix is austenite, while for group 3, the matrix is primarily a ferrite phase. It should be noted that these areas of deposited metal have the greatest resistance to abrasive wear, as indicated by the value of the abrasion damage tolerance index $1/(E^2\cdot H)$.

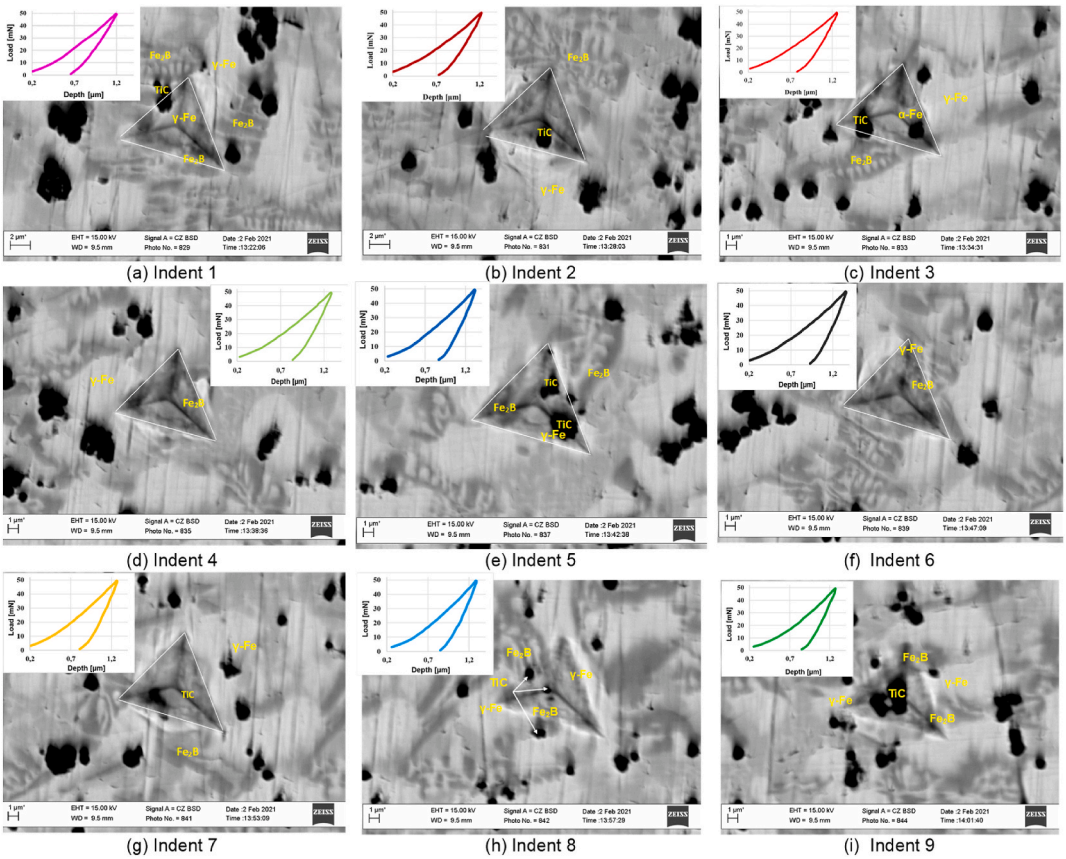

Fig. 11. Indentation marks and their load-depth dependence curves for different sections of the deposited metal, each shown in Fig. 10: (a)-Indent 1; (b)-Indent 2; (c)-Indent 3; (d)-Indent 4; (e)-Indent 5; (f)-Indent 6; (g)-Indent 7; (h)-Indent 8; (i)-Indent 9.

Analytical methods for solving singular problems about the stress state of coatings under local load in relation to the problems of indentation and interaction with abrasive particles are proposed in papers [185–187]. Later, these approaches were developed to model the behavior of layered [188,189] and functionally gradient [190] coatings.

In the following work, it is planned to investigate the influence of copper addition on the mechanical properties of the Fe–Cr–C–B–Ti–Cr boron alloy of the alloying system, the abrasive wear resistance and tribocorrosion wear.

4. Conclusions

The article considered the possibility of applying to alloys deposited by hardfacing process (characterized by non-equilibrium conditions) modern software products (Thermo-Calc, JMatPro) for predicting the phase composition and chemical composition of the resulting phases, as well as a computation complex for calculating mechanical properties. The main conclusions are as follows.

1. In the process of equilibrium cooling the precipitation of the experimental steel, the precipitation order of phase is TiC → γ–Fe → Fe_2B →Cu → Cr_7C_3 → CrFeB → α–Fe. The primary phases are the phases of titanium carbide, austeite and hemiboride $(Fe, Cr)_2B$. Moreover, the first phase that will be formed in the liquid solution will be titanium carbide.
2. Analysis of the alloying elements distribution in the deposited metal showed that such alloying elements as Cu, Si, Al were concentrated mainly in the matrix, since chromium was concentrated mostly in borides. Whereas titanium was contained entirely in own TiC carbides. It was also confirmed by thermodynamic calculations, EDS mapping analysis and electron breakdown microanalyzer (EPMA)
3. γ–Fe+Cr_7C_3 eutectic was found in the alloys subject to research as a matrix, a $M_2(B,C)$, borocarbides skeleton, as well as $M_3(B,C)$ (M = Fe, Cr, Mo, V, Mn).
4. Cu phase was not observed as individual particles in deposited metal due to the significant solubility of copper in the residual austenite. It was formed in the deposited metal due to the impossibility of achieving a stable state of the metal during welding.
5. EDX analysis data and his typical EDX spectra showed that typical phases in the alloy were as follows: γ–Fe (austenite), hemiboride $Fe_{1.8}Cr_{0.2}B$, borcementite $(Fe_{2.5}Cr_{0.5})(B_{0.5}C_{0.5})$, and titanium carbides $(Ti_{0.81}Fe_{0.19})C$.

6. First principles calculations using density functional theory (DFT) were performed to study the mechanical properties of phases (γ–Fe (austenite), hemioboride $Fe_{1.8}Cr_{0.2}B$, boron cementite $(Fe_{2.5}Cr_{0.5})(B_{0.5}C_{0.5})$, and titanium carbide $((Ti_{0.81}Fe_{0.19})C)$ in the deposited metal 110Cr4Cu7Ti1VB. Pugh's ratio had the highest value $k = G/B = 0.65$ for it, while hemioboride Fe_2B and borcementite $Fe_3(B,C)$ were plastic phases $G/B = 0.37 < 0.571$. The most plastic phase were the austenitic phases. At the same time, the titanium carbide phase had the highest microhardness, due to the dominant covalent bond type, confirmed by the high values of Cauchy pressure $p_C = -57 < 0$.
7. We determined mechanical properties of deposited metal areas with different phase composition, using microindentation method. The areas of deposited metal with boride and carboboride eutectics were the most wear resistant. Whereas areas of the deposited metal with titanium carbides showed less resistance to abrasive wear due to the brittle failure tendency, despite high values of microhardness.

Funding

This study was carried out as part of the project "Belt and Road Initiative Centre for Chinese-European studies (BRICES)" and was funded by the Guangdong University of Petrochemical Technology.

Data availability statement

Data used in this research will be made available upon reasonable request.

CRediT authorship contribution statement

Vasyl Lozynskyi: Writing – original draft, Supervision, Funding acquisition, Formal analysis. **Bohdan Trembach:** Writing – review & editing, Writing – original draft, Visualization, Software, Resources, Project administration, Methodology, Investigation, Funding acquisition, Formal analysis, Conceptualization. **Md Mukter Hossain:** Software, Methodology, Investigation, Formal analysis, Data curation. **Mohammad Humaun Kabir:** Software, Methodology, Investigation, Data curation. **Yury Silchenko:** Writing – original draft, Supervision. **Michal Krbata:** Validation, Software, Methodology, Investigation, Data curation. **Kostiantyn Sadovyi:** Writing – review & editing. **Oleksii Kolomiitse:** Writing – review & editing. **Liubomyr Ropyak:** Writing – review & editing, Writing – original draft, Visualization, Validation, Supervision, Project administration, Methodology, Formal analysis.

Declaration of competing interest

The authors declare that they have no known competing financial interests or personal relationships that could have appeared to influence the work reported in this paper.

Acknowledgments

The authors are grateful to the Ministry of Science and Education of Ukraine for the grant to implement projects 0122U002082 and 0123U101858. The team of authors expresses their gratitude to the reviewers for valuable recommendations that have been taken into account to improve significantly the quality of this paper. The team of authors thanks Irinayu Litwinyuk for her help in translating the article and editing the text.

References

[1] K. Holmberg, A. Erdemir, Influence of tribology on global energy consumption, costs and emissions, Friction 5 (2017) 263–284, https://doi.org/10.1007/s40544-017-0183-5.
[2] B.O. Trembach, M.G. Sukov, V.A. Vynar, I.O. Trembach, V.V. Subbotina, O. Yu Rebrov, O.M. Rebrova, V.I. Zakiev, Effect of incomplete replacement of Cr for Cu in the deposited alloy of Fe–C–Cr–B–Ti alloying system with a medium boron content (0.5% wt.) on its corrosion resistance, Metallofiz. Noveishie Tekhnol. 44 (2022) 493, https://doi.org/10.15407/mfint.44.04.0493, 413.
[3] I.P. Shatskii, Tension of a plate containing a rectilinear cut with hinged rims, J. Appl. Mech. Tech. Phys. 30 (1989) 828–830, https://doi.org/10.1007/BF00851435.
[4] I.P. Shats'kyi, M.V. Makoviichuk, Contact interaction of the crack edges in the case of bending of a plate with elastic support, Mater. Sci. 39 (2003) 371–376, https://doi.org/10.1023/B:MASC.0000010742.15838.44.
[5] S. Mohammadi, M. Yousefi, M. Khazaei, A review on composite patch repairs and the most important parameters affecting its efficiency and durability, J. Reinf. Plast. Compos. 40 (2020) 3–15, https://doi.org/10.1177/0731684420941602.
[6] W.K. Ahmed, A.-H.I. Mourad, Strengthening of misaligned welded pipes with outer circumferentially crack using FRP bandage finite element analysis, J. Mech. Eng. Technol. 1 (2013) 66–73, https://doi.org/10.18005/JMET010200.
[7] I. Shats'kyi, M. Makoviichuk, A. Shcherbii, Influence of a flexible coating on the strength of a shallow cylindrical shell with longitudinal crack, J. Math. Sci. 238 (2019) 165–173, https://doi.org/10.1007/s10958-019-04226-9.
[8] I.P. Shatskyi, M.V. Makoviichuk, A.B. Shcherbii, Influence of flexible coating on the limit equilibrium of a spherical shell with meridional crack, Mater. Sci. 55 (2020) 484–491, https://doi.org/10.1007/s11003-020-00329-w.
[9] M. Dutkiewicz, T. Dalyak, I. Shatskyi, T. Venhrynyuk, A. Velychkovych, Stress analysis in damaged Pipeline with composite coating, Appl. Sci. 11 (2021) 10676, https://doi.org/10.3390/app112210676.
[10] P. Shats'kyi, Limiting equilibrium of a plate with partially healed crack, Mater. Sci. 51 (2015) 322–330, https://doi.org/10.1007/s11003-015-9845-5.
[11] I.P. Shatskyi, V.V. Perepichka, L.Y. Ropyak, On the influence of facing on strength of solids with surface defects, Metallofiz. Noveishie Tekhnol. 42 (2020) 69–76, https://doi.org/10.15407/mfint.42.01.0069.

[12] G.S. Abdelhaffez, H.M. Ahmed, H.A. Saleem, Effect of ore heterogeneity on the ball mill wear rate during a grinding process at gold mines of Saudi Arabia (KSA), Min. Miner. Depos. 17 (2023) 71–81, https://doi.org/10.33271/mining17.02.071.

[13] V. Yanchuk, I. Kruhlov, V. Zakiev, A. Lozova, B. Trembach, A. Orlov, S. Voloshko, Thermal and ion treatment effect on nanoscale thin films scratch resistance, Metallofiz. Noveishie Tekhnol. 44 (2022) 1275–1292, https://doi.org/10.15407/mfint.44.10.1275.

[14] O. Ivanov, P. Prysyazhnyuk, L. Shlapak, S. Marynenko, L. Bodrova, H. Kramar, Researching of the structure and properties of FCAW hardfacing based on Fe–Ti–Mo–BC welded under low current, Procedia Struct. Integr. 36 (2022) 223–230, https://doi.org/10.1016/j.prostr.2022.01.028.

[15] O. Bazaluk, A. Velychkovych, L. Ropyak, M. Pashechko, T. Pryhorovska, V. Lozynskyi, Influence of heavy weight drill pipe material and drill bit manufacturing errors on stress state of steel blades, Energies 14 (2021) 4198, https://doi.org/10.3390/en14144198.

[16] D. Ulbrich, M. Kańczurzewska, Correlation tests of ultrasonic wave and mechanical parameters of spot-welded joints, Materials 15 (2022) 1–23, https://doi.org/10.3390/ma15051701.

[17] D. Ulbrich, J. Kowalczyk, M. Jósko, W. Sawczuk, P. Chudyk, Assessment of selected properties of varnish coating of motor vehicles, Coatings 11 (2021) 1–18, https://doi.org/10.3390/coatings11111320.

[18] Y. Kusyi, V. Stupnytskyy, O. Onysko, E. Dragašius, S. Baskutis, R. Chatys, Optimization synthesis of technological parameters during manufacturing of the parts, Eksploatacja i Niezawodność – Maintenance and Reliability 24 (2022) 655–667, https://doi.org/10.17531/ein.2022.4.6.

[19] O. Bazaluk, O. Dubei, L. Ropyak, M. Shovkoplias, T. Pryhorovska, V. Lozynskyi, Strategy of compatible use of jet and plunger pump with chrome parts in oil well, Energies 15 (2022) 83, https://doi.org/10.3390/en15010083.

[20] M. Dutkiewicz, A. Velychkovych, I. Shatskyi, V. Shopa, Efficient model of the interaction of elastomeric filler with an open shell and a chrome-plated shaft in a dry friction damper, Materials 15 (2022) 4671, https://doi.org/10.3390/ma15134671.

[21] M. Storchak, I. Zakiev, V. Zakiev, A. Manokhin, Coatings strength evaluation of cutting inserts using advanced multi-pass scratch method, Measurement 191 (2022) 110745, https://doi.org/10.1016/j.measurement.2022.110745.

[22] V.I. Bolshakov, A.V. Kalinin, D.B. Hlushkova, A.I. Voronkov, I.N. Nikitchenko, Structural materials modification during plasmochemical synthesis enriched with nanoparticles, Probl. At. Sci. Technol. 117 (2018) 97–102.

[23] V. Pidkova, I. Brodnikovska, Z. Duriagina, V. Petrovskyy, Structure and properties of Mg, Al, Ti oxide and nitride layers formed by ion-plasma sputtering, Met. Funct. Mater. 22 (2014) 34–39, https://doi.org/10.15407/fm22.01.034.

[24] D.B. Hlushkova, V.M. Volchuk, P.M. Polyansky, V.A. Saenko, A.A. Efimenko, Fractal modeling the mechanical properties of the metal surface after ion-plasma chrome plating, Met. Funct. Mater. 30 (2023) 275–281, https://doi.org/10.15407/fm30.02.275.

[25] O.V. Sukhova, Structure and properties of Fe–B–C powders alloyed with Cr, V, Mo or Nb for plasma-sprayed coatings, Probl. At. Sci. Technol. 128 (2020) 77–83. https://vant.kipt.kharkov.ua/TABFRAME2.html.

[26] Y. Dilay, B. Güney, A. Özkan, A. Öz, Microstructure and wear properties of WC–10Co–4Cr coating to cultivator blades by DJ-HVOF, Emerg. Mater. Res. 10 (2021) 278–288, https://doi.org/10.1680/jemmr.20.00324.

[27] B. Güney, Y. Dilay, Determination of abrasion resistance of Fe28Cr5C1Mn coating applied to 30MnB5 boron alloy cultivator blades via electric arc spray, Proc. Inst. Mech. Eng. C: J. Mech. Eng. Sci. (2022), https://doi.org/10.1177/09544062221097803, 236 9687-9699.

[28] D.B. Hlushkova, V.A. Bagrov, S.V. Demchenko, V.M. Volchuk, O.V. Kalinin, N.E. Kalinina, Structure and properties of powder gas-plasma coatings based on nickel, Probl. At. Sci. Technol. 140 (2022) 125–130, https://doi.org/10.46813/2022-140-125.

[29] M.M. Student, V.M. Dovhunyk, V.M. Posuvailo, Friction behavior of iron-carbon alloys in couples with plasma-electrolytic oxide-ceramic layers synthesized on D16T alloy, Mater. Sci. 53 (2017) 359–367, https://doi.org/10.1007/s11003-017-0083-x.

[30] V.S. Vahrusheva, D.B. Hlushkova, V.M. Volchuk, T.V. Nosova, S.I. Mamhur, N.I. Tsokur, V.A. Bagrov, S.V. Demchenko, YuV. Ryzhkov, V.O. Scrypnikov, Increasing the corrosion resistance of heat-resistant alloys for parts of power equipment, Probl. At. Sci. Technol. 140 (2022) 137–140, https://doi.org/10.46813/2022-140-137.

[31] M. Khoma, V. Vynar, C. Vasyliv, B. Datsko, M. Golovchuk, Influence of heat treatment of 30MnB5 steel on its micromechanical properties and resistance to abrasion wear, Tribol. Ind. 44 (2022) 310–321, https://doi.org/10.24874/ti.1146.06.21.02.

[32] D. Ulbrich, A. Stachowiak, J. Kowalczyk, D. Wieczorek, W. Matysiak, Tribocorrosion and abrasive wear test of 22MnCrB5 hot-formed steel, Materials 15 (2022) 3892, https://doi.org/10.3390/ma15113892.

[33] L. Ropyak, T. Shihab, A. Velychkovych, V. Bilinskyi, V. Malinin, M. Romaniv, Optimization of plasma electrolytic oxidation technological parameters of deformed aluminum alloy D16T in flowing electrolyte, Ceramics 6 (2023) 146–167, https://doi.org/10.3390/ceramics6010010.

[34] L. Ropyak, T. Shihab, A. Velychkovych, O. Dubei, T. Tutko, V. Bilinskyi, Design of a two-layer Al–Al_2O_3 coating with an oxide layer formed by the plasma electrolytic oxidation of Al for the corrosion and wear protections of steel, Progress in Physics of Metals 24 (2023) 319–365, https://doi.org/10.15407/ufm.24.02.319.

[35] O. Sobol, A. Andreev, V. Stolbovoy, S. Knyazev, A. Barmin, N. Krivobok, Study of the effect of ion nitriding regimes on the structure and hardness of steel, East.-Eur. J. Enterp. Technol. 2 (2016) 63–68, https://doi.org/10.15587/1729-4061.2016.63659.

[36] L. Ma, C. Huang, J. Jiang, R. Hui, Y. Xie, Z.S. Liu, Cracks formation and residual stress in chromium carbide overlays, Eng. Fail. Anal. 31 (2013) 320–337, https://doi.org/10.1016/j.engfailanal.2013.01.050.

[37] P. Prysyazhnyuk, M. Molenda, T. Romanyshyn, L. Ropyak, L. Romanyshyn, V. Vytvytskyi, Development of a hardbanding material for drill pipes based on high-manganese steel reinforced with complex carbides, Acta Montan. Slovaca 27 (2022) 685–696, https://doi.org/10.46544/AMS.v27i3.09.

[38] W. Wu, L.Y. Hwu, D.Y. Lin, J.L. Lee, The relationship between alloying elements and retained austenite in martensitic stainless steel welds, Scr. Mater. 42 (2000) 1071–1076, https://doi.org/10.1016/S1359-6462(00)00339-0.

[39] O. Ivanov, P. Prysyazhnyuk, L. Romanyshyn, T. Romanyshyn, Y. Mosora, Using FCAW with electrodes based on Fe–Ti–Mo–BC system for increasing of durability of junk removal tools, Multidiscip. Asp. Prod. Eng. 4 (2021) 132–141, https://doi.org/10.2478/mape-2021-0012.

[40] M. Bembenek, P. Prysyazhnyuk, T. Shihab, R. Machnik, O. Ivanov, L. Ropyak, Microstructure and wear characterization of the Fe–Mo–B–C-based hardfacing alloys deposited by flux-cored arc welding, Materials 15 (2022) 5074, https://doi.org/10.3390/ma15145074.

[41] E. Kocaman, B. Kılınç, M. Durmaz, Ş. Şen, U. Şen, The influence of chromium content on wear and corrosion behavior of surface alloyed steel with $Fe_{(16-x)}Cr_x(B,C)_4$ electrode, Eng. Sci. Technol. Int. J. 24 (2021) 533–542, https://doi.org/10.1016/j.jestch.2020.08.003.

[42] E. Kocaman, B. Kılınç, Ş. Şen, U. Şen, Development of surface properties with in situ TiB_2 intermetallic-assisted coating by $Fe_{(18-X)}Ti_2B_X$ (x = 3,4,5)-based electrodes, Arab. J. Sci. Eng. 47 (2022) 8485–8501, https://doi.org/10.1007/s13369-021-06304-0.

[43] J. Pawlik, J. Cieślik, M. Bembenek, T. Góral, S. Kapayeva, M. Kapkenova, On the influence of linear energy/heat input coefficient on hardness and weld bead geometry in chromium-rich stringer GMAW coatings, Materials 15 (2022) 6019, https://doi.org/10.3390/ma15176019.

[44] J. Pawlik, M. Bembenek, T. Góral, J. Cieślik, J. Krawczyk, A. Łukaszek-Sołek, T. Śleboda, Ł. Frocisz, On the influence of heat input on Ni-wc GMAW hardfaced coating properties, Materials 16 (2023) 3960, https://doi.org/10.3390/ma16113960.

[45] B. Kılınç, E. Kocaman, Ş. Şen, U. Şen, Effect of titanium content on the microstructure and wear behavior of $Fe_{(13-x)}TixB_7$ (x= 0–5) hardfacing alloy, J. Min. Metall. B Metall. 58 (2021) 29–41, https://doi.org/10.2298/JMMB210430047K.

[46] M. Krbata, R. Ciger, M. Kohutiar, M. Eckert, I. Barenyi, B. Trembach, A. Dubec, J. Escherova, M. Gavalec, N. Beronská, Microstructural changes and determination of a continuous cooling transformation (CCT) diagram using dilatometric analysis of M398 high-alloy tool steel produced by microclean powder metallurgy, Materials 16 (2023) 4473, https://doi.org/10.3390/ma16124473.

[47] E. Kocaman, B. Kılınç, Ş. Şen, U. Şen, In-situ TiB_2 and Fe_2Ti intermetallic assisted hard coatings by Fe–Ti–B based hardfacing electrodes, J. Alloys Compd. 900 (2022) 163478, https://doi.org/10.1016/j.jallcom.2021.163478.

[48] B.O. Trembach, D.V. Hlushkova, V.M. Hvozdetskyi, V.A. Vynar, V.I. Zakiev, O.V. Kabatskyi, D.V. Savenok, O.Yu Zakavorotnyi, Prediction of fill factor and charge density of self-shielding flux-cored wire with variable composition, Mater. Sci. 59 (2023), https://doi.org/10.1007/s11003-023-00738-7.

[49] B. Trembach, A. Grin, M. Turchanin, O. Markov, I. Trembach, Application of taguchi method and ANOVA analysis for optimization of process parameters and exothermic addition (CuO-Al) introduction in the core filler during self-shielded flux-cored arc welding, Int. J. Adv. Manuf. Technol. 114 (2021) 1099–1118, https://doi.org/10.1007/s00170-021-06869-y.

[50] J.G.F. Júnior, A.H.C. Cardoso, A.Q. Bracarense, Effects of TiC formation in situ by applying titanium chips and other ingredients as a flux of tubular wire, J. Braz. Soc. Mech. Sci. Eng. 42 (2020) 375, https://doi.org/10.1007/s40430-020-02462-8.

[51] J.G. Fagundes Júnior, A.H.C. Cardoso, A.Q. Bracarense, Addition of TiO_2, $CaCO_3$ and CaF_2 as a flux of tubular wire applied for TiC in-situ reaction, Soldagem Inspeção 25 (2020) e2511, https://doi.org/10.1590/0104-9224/SI25.11.

[52] B. Trembach, O. Balenko, V. Davydov, V. Brechko, I. Trembach, O. Kabatskyi, Prediction the melting characteristics of flux-cored wire with exothermic addition (CuO–Al), in: 2022 *IEEE International Conference On Modern Electrical And Energy Systems (MEES)*, 20–23 October 2022, Kremenchuk, Ukraine, IEEE Xplore, Kremenchuk, Ukraine, 2022, pp. 641–647, https://doi.org/10.1109/MEES58014.2022.10005657.

[53] J.C. Buchely, L.M. Gutierrez, L.M. León, A. Toro, The effect of microstructure on abrasive wear of hardfacing alloys, Wear 259 (2005) 52–61, https://doi.org/10.1016/j.wear.2005.03.002.

[54] M. Orečny, M. Buršak, J. Viňaš, The influence of heat treatment on the abrasive wear resistance of a construction and a tool steel, Metalurgija 54 (2015) 91–193.

[55] A. Wiengmoon, Carbides in high chromium cast irons, Naresuan Univ. Eng. J. 6 (2011) 64–71, https://doi.org/10.14456/nuej.2011.6.

[56] C. Fan, M.C. Chen, C.M. Chang, W. Wu, Microstructure change caused by $(Cr, Fe)_{23}C_6$ carbides in high chromium Fe–Cr–C hardfacing alloys, Surf. Coat. Technol. 201 (2006) 908–912, https://doi.org/10.1016/j.surfcoat.2006.01.010.

[57] A. Jilleh, N.K. Babu, V. Thota, M.K. Harun, M.K. Talari, Microstructural and mechanical properties investigation of TiC reinforced hardface alloy deposited on mild steel substrate, Trans. Indian Inst. Met. 66 (2013) 433–436, https://doi.org/10.1007/s12666-013-0252-z.

[58] Y. Jian, H. Ning, Z. Huang, Y. Wang, J. Xing, Three-body abrasive wear behaviors and mechanism analysis of Fe–B–C cast alloys with various Mn contents, J. Mater. Res. Technol. 14 (2021) 1301–1311, https://doi.org/10.1007/s12666-013-0252-z.

[59] J. Lentz, A. Röttger, W. Theisen, Solidification and phase formation of alloys in the hypoeutectic region of the Fe–C–B system, Acta Mater. 99 (2015) 119–129, https://doi.org/10.1016/j.actamat.2015.07.037.

[60] P. Prysyazhnyuk, D. Di Tommaso, The thermodynamic and mechanical properties of Earth-abundant metal ternary boride $Mo_2(Fe,Mn)B_2$ solid solutions for impact- and wear-resistant alloys, Mater. Adv. 4 (2023) 3822–3838, https://doi.org/10.1039/D3MA00313B.

[61] E.V. Sukhova, The effect of carbon content and cooling rate on the structure of boron-rich Fe–B–C alloys, Phys. Chem. Solid State 21 (2020) 355–360, https://doi.org/10.15330/pcss.21.2.355-360.

[62] N.Y. Filonenko, O.M. Galdina, Effect of carbon on the physical and structural properties of boride Fe_2B, Phys. Chem. Solid State 17 (2016) 251–255, https://doi.org/10.15330/pcss.17.2.251-255.

[63] N. Yüksel, S. Şahin, Wear behavior–hardness–microstructure relation of Fe–Cr–C and Fe–Cr–C–B based hardfacing alloys, Materials & design 58 (2014) 491–498, https://doi.org/10.1016/j.matdes.2014.02.032.

[64] J. Lentz, A. Röttger, W. Theisen, Hardness and modulus of Fe_2B, $Fe_3(C,B)$, and $Fe_{23}(C,B)6$ borides and carboborides in the Fe–C–B system *Mater*, Charact 135 (2017) 192–202, https://doi.org/10.1016/j.matchar.2017.11.012.

[65] E.V. Sukhova, Effect of Ti, Al, Si on the structure and mechanical properties of boron-rich Fe–B–C alloys, East Eur. J. Phys. 2 (2021) 115–121, https://doi.org/10.26565/2312-4334-2021-2-08.

[66] B. Nedeljković, V. Lazić, S. Aleksandrović, B. Krstić, M. Mutavdžić, D. Milosavljević, M. Đorđević, Influence of the carbide type on tribological properties of the hardfaced layers, Metalurgija–J. Metall. 16 (2010) 77–90.

[67] X. Wei, Z. Chen, J. Zhong, L. Wang, W. Yang, Y. Wang, Effect of alloying elements on mechanical; electronic and magnetic properties of Fe_2B by first-principles investigations, Comput. Mater. Sci. 147 (2018) 322–330, https://doi.org/10.1016/j.commatsci.2018.02.001.

[68] J. Lentz, A. Röttger, W. Theisen, Microstructures, heat treatment, and properties of boron-alloyed tool steels, Steel Res. Int. 91 (2020) 1900416, https://doi.org/10.1002/srin.201900416.

[69] P. Prysyazhnyuk, L. Shlapak, I. Semyanyk, V. Kotsyubynsky, L. Troshchuk, S. Korniy, V. Artym, Analysis of the effects of alloying with Si and Cr on the properties of manganese austenite based on ab initio modelling, E. Eur. J. Enterprise Technol. 6 (2020) 28–36, https://doi.org/10.15587/1729-4061.2020.21728.

[70] P.M. Prysyazhnyuk, T.A. Shihab, V.H. Panchuk, Formation of the structure of Cr_3C_2–MNMts 60–20–20 cermets, Mater. Sci. 52 (2016) 188–193, https://doi.org/10.1007/s11003-016-9942-0.

[71] J. You, H.G. Kim, J. Lee, H.H. Kim, Y. Cho, B.S. Jeong, S.H. Hong, Effects of molybdenum addition on microstructure and mechanical properties of Fe-B-C sintered alloys, Mater. Charact. 173 (2021) 110915, https://doi.org/10.1016/j.matchar.2021.110915.

[72] M.R. Tavakoli Shoushtari, M. Goodarzi, H. Sabet, Investigation of microstructure; and dry sliding wear of hardfaced layers produced by FCAW using cored wire Fe–B–C–Ti alloy, Iran. J. Mater. Sci. Eng. 15 (2018) 19–32, https://doi.org/10.22068/ijmse.15.4.19.

[73] Z. Lv, H. Fu, J. Xing, S. Ma, Y. Hu, Microstructure and crystallography of borides and mechanical properties of Fe–B–C–Cr–Al alloys, J. Alloys Compd. 662 (2016) 54–62, https://doi.org/10.1016/j.jallcom.2015.11.171.

[74] O.V. Sukhova, Solubility of Cu, Ni, Mn in boron-rich Fe-B-C alloys, Phys. Chem. Solid. State. 22 (2021) 110–116, https://doi.org/10.15330/pcss.22.1.110-116.

[75] S.I. Ryabtsev, V.A. Polonskyy, O.V. Sukhova, Structure and corrosion of quasicrystalline cast alloys and Al–Cu–Fe film coatings, Mater. Sci. 56 (2020) 263–272. %2010.1007/s11003-020-00428-8.

[76] Y. Yi, J. Xing, M. Wan, L. Yu, Y. Lu, Y. Jian, Effect of Cu on microstructure; crystallography and mechanical properties in Fe-B-C-Cu alloys, Mater. Sci. Eng. A 708 (2017) 274–284, https://doi.org/10.1016/j.msea.2017.09.135.

[77] O. Ozdemir, M. Usta, C. Bindal, A.H. Ucisik, Hard iron boride (Fe_2B) on 99.97 wt% pure iron, Vacuum 80 (2006) 1391–1395, https://doi.org/10.1016/j.vacuum.2006.01.022.

[78] M.S. Li, X.L. Fu, W.D. Xu, R.L. Zhang, R.H. Yu, Valence electron structure of Fe_2B phase and its eigen-brittleness, Acta Metall. Sin. 31 (1995) 201–208.

[79] I. Kirkovska, V. Homolová, I. Petryshynets, T. Csanádi, The influence of the third element on nano-mechanical properties of iron borides FeB and Fe_2B formed in Fe–B–X (X = C, Cr, Mn, V, W, Mn + V) alloys, Materials 13 (2020) 4155, https://doi.org/10.3390/ma13184155.

[80] H. Berns, A. Fischer, Microstructure of Fe–Cr–C hardfacing alloys with additions of Nb, Ti and B, Mater. Charact. 39 (1997) 499–527, https://doi.org/10.1016/S1044-5803(97)00142-3.

[81] Y. Jian, Z. Huang, J. Xing, B. Wang, Effects of chromium addition on fracture toughness and hardness of oriented bulk Fe_2B crystals, Mater. Charact. 110 (2015) 138–144, https://doi.org/10.1016/j.matchar.2015.10.017.

[82] Y. Jian, Z. Huang, J. Xing, X. Guo, Y. Wang, Z. Lv, Effects of Mn addition on the two-body abrasive wear behavior of Fe–3.0 wt% B alloy, Tribol. Int. 103 (2016) 243–251, https://doi.org/10.1016/j.triboint.2016.07.008.

[83] M.I. Pashechko, J. Montusiewicz, Evaluation of the wear resistance of eutectic coatings of the Fe–Mn–C–B system alloyed by Si, Ni, and Cr using multi-criteria analysis, Mater. Sci. 47 (2012) 813–821, https://doi.org/10.1007/s11003-012-9460-7.

[84] Z. Huang, J. Xing, X. Tao, Effect of molybdenum addition on fracture toughness and hardness of Fe2B in Fe-B-C cast alloy, Int. J. Mater. Res. 103 (2012) 1539–1543, https://doi.org/10.3139/146.110826.

[85] C. Badini, C. Gianoglio, G. Pradelli, The effect of carbon; chromium and nickel on the hardness of borided layers, Surf. Coat. Tech. 30 (1987) 157–170, https://doi.org/10.1016/0257-8972(87)90140-X.

[86] Y.A. Balandin, Surface hardening of die steels by diffusion boronizing; borocopperizing; and borochromizing in fluidized bed, Met. Sci. Heat. Treat. 47 (2005) 103–106, https://doi.org/10.1007/s11041-005-0037-z.

[87] B. Trembach, A. Grin, V. Subbotina, V. Vynar, S. Knyazev, V. Zakiev, O. Kabatskyi, Effect of exothermic addition (CuO-Al) on the structure; mechanical properties and abrasive wear resistance of the deposited metal during self-shielded flux-cored arc welding, Tribol. Ind. 43 (2021) 452–464, https://doi.org/10.24874/ti.1104.05.21.07.

[88] O.V. Sukhova, Physical-and-chemical processes at the interfaces of (Cu–Ni–Mn–Fe)/(W–C) composites, Lith. J. Phys. 1 (2023) 15–24, https://doi.org/10.3952/physics.2023.63.1.3.

[89] E. Albertin, A. Sinatora, Effect of carbide fraction and matrix microstructure on the wear of cast ion balls tested in a laboratory ball mill, Wear 250 (2001) 492–501, https://doi.org/10.1016/S0043-1648(01)00664-0.

[90] N. Espallargas, P.D. Jakobsen, L. Langmaack, F.J. Macias, Influence of corrosion on the abrasion of cutter steels used in TBM tunnelling, Rock Mech. Rock Eng. 48 (2015) 261–275, https://doi.org/10.1007/s00603-014-0552-6.

[91] P. Prysyazhnyuk, D. Lutsak, A. Vasylyk, S. Taer, M. Burda, Calculation of surface tension and its temperature dependence for liquid Cu–20Ni–20Mn alloy, Metall. Min. Ind. 7 (2015) 346–350.

[92] A. Sundström, J. Rendón, M. Olsson, Wear behaviour of some low alloyed steels under combined impact/abrasion contact, Wear 250–251 (2001) 744–754, https://doi.org/10.1016/S0043-1648(01)00712-8.

[93] A.K. Jha, B.K. Prasad, O.P. Modi, S. Das, A.H. Yegneswaran, Correlating microstructural features and mechanical properties with abrasion resistance of a high strength low alloy steel, Wear 254 (2003) 120–128, https://doi.org/10.1016/S0043-1648(02)00309-5.

[94] J.W. Yoo, S.H. Lee, C.S. Yoon, S.J. Kim, The effect of boron on the wear behavior of iron-based hardfacing alloys for nuclear power plants valves, J. Nucl. Mater. 352 (2006) 90–96, https://doi.org/10.1016/j.jnucmat.2006.02.071.

[95] Y. Jian, J. Xing, Z. Huang, T. Wu, Quantitative characterization of the wear interactions between the boride and metallic matrix in Fe-3.0 wt% B duplex alloy, Wear 436 (2019) 203021, https://doi.org/10.1016/j.wear.2019.203021.

[96] Z. Liu, Y. Li, X. Chen, K. Hu, Microstructure and mechanical properties of high boron white cast iron, Mater. Sci. Eng. A 486 (2008) 112–116, https://doi.org/10.1016/j.msea.2007.10.017.

[97] C. Guo, P.M. Kelly, Boron solubility in Fe–Cr–B cast irons, Mater. Sci. Eng. A 352 (2003) 40–45, https://doi.org/10.1016/S0921-5093(02)00449-5.

[98] G. Laird, G.L. Powell, Solidification and solid-state transformation mechanisms in Si alloyed high-chromium white cast irons, Metall. Trans. A 24 (1993) 981–988, https://doi.org/10.1007/BF02656520.

[99] H. Ohtsuka, Effects of Cu on diffusional transformation behaviour and microstructure in Fe–Mn–Si–C steels, ISIJ Int. 37 (1997) 296–301, https://doi.org/10.2355/isijinternational.37.296.

[100] M. Krbaťa, M. Eckert, R. Cíger, M. Kohutiar, Physical modeling of CCT diagram of tool steel 1.2343, Procedia Struct. Integr. 43 (2023) 270–275, https://doi.org/10.1016/j.prostr.2022.12.270.

[101] J. Banas, A. Mazurkiewicz, The effect of copper on passivity and corrosion behaviour of ferritic and ferritic–austenitic stainless steels, Mater. Sci. Eng. A. 277 (2000) 183–191, https://doi.org/10.1016/S0921-5093(99)00530-4.

[102] N.D. Greene, C.R. Bishop, M. Stern, Corrosion and electrochemical behavior of chromium-noble metal alloys, J. Electrochem. Soc. 108 (1961) 836–841, https://doi.org/10.1149/1.2428234.

[103] J. Wang, C. Li, X. Di, D. Wang, Effect of Cu content on microstructure and mechanical properties for high-strength deposited metals strengthened by nano-precipitation, Metals 12 (2022) 1360, https://doi.org/10.3390/met12081360.

[104] J. Wang, X. Di, C. Li, D. Wang, Characterization of nanoscale precipitates and enhanced mechanical properties of high strength weld metals containing Cu additions after PWHT, Metall. Res. Technol. 119 (2022) 119, https://doi.org/10.1051/metal/2022007.

[105] E.J. Czyryca, M.G. Vassilaros, Advances in low carbon; high strength ferrous alloys, J. Chem. Inf. Model. 92 (1993) 1–44.

[106] H. Kong, Z. Jiao, J. Lu, C.T. Liu, Low-carbon advanced nanostructured steels: microstructure, mechanical properties, and applications, Sci. China Mater. 64 (2021) 1580–1597, https://doi.org/10.1007/s40843-020-1595-2.

[107] H. Yu, Z. Luo, Y. Feng, Z. Liu, G. Xie, R.D.K. Misra, Effect of Cu additions on the microstructure, wear resistance and corrosion resistance of Fe-based/B_4C composite coating by vacuum cladding, Surf. Coat. Technol. 454 (2023) 12919, https://doi.org/10.1016/j.surfcoat.2022.129191.

[108] J. Viňáš, L. Kaščák, Possibilities of using welding-on technologies in crane wheel renovation, Bull. Mater. Sci. 31 (2008) 125–131, https://doi.org/10.1007/s12034-008-0022-4.

[109] Y. Vynnykov, M. Kharchenko, S. Manhura, H. Muhlis, A. Aniskin, A. Manhura, Analysis of corrosion fatigue steel strength of pump rods for oil wells, Min. Miner. Depos. 16 (2022) 31–37, https://doi.org/10.33271/mining16.03.031.

[110] J. Selech, D. Ulbrich, D. Romek, J. Kowalczyk, K. Wlodarczyk, K. Nadolny, Experimental study of abrasive; mechanical and corrosion effects in ring-on-ring sliding contact, Materials 13 (2020) 4950, https://doi.org/10.3390/ma13214950.

[111] J. Viňáš, J. Brezinová, J. Brezina, P. Hermel, Innovation of biomass crusher by application of hardfacing layers, Metals 11 (2021) 1283, https://doi.org/10.3390/met11081283.

[112] D.B. Hlushkova, V.A. Bagrov, V.M. Volchuk, U.A. Murzakhmetova, Influence of structure and phase composition on wear resistance of sparingly alloyed alloys, Met. Funct. Mater. 30 (2023) 74–78, https://doi.org/10.15407/fm30.01.74.

[113] S.V. Zharikov, A.G. Grin, Investigation of slags in surfacing with exothermic flux-cored wires, Weld. Int. 29 (2015) 386–389, https://doi.org/10.1080/09507116.2014.934538.

[114] A.F. Vlasov, N.A. Makarenko, A.M. Kushchiy, Using exothermic mixtures in manual arc welding and electroslag processes, Weld. Int. 31 (2017) 565–570, https://doi.org/10.1080/09507116.2017.1295561.

[115] A.F. Vlasov, N.A. Makarenko, Special features of heating and melting electrodes with an exothermic mixture in the coating, Weld. Int. 30 (2016) 717–722, https://doi.org/10.1080/09507116.2016.1143586.

[116] V.V. Chigarev, D.A. Zarechenskii, A.G. Belik, Optimisation of the composition and melting parameters of powder strips with the exothermic mixture in the filler, Weld. Int. 30 (2016) 557–559, https://doi.org/10.1080/09507116.2015.1099892.

[117] J. Kowalczyk, W. Matysiak, W. Sawczuk, D. Wieczorek, K. Sędłak, M. Nowak, Quality tests of hybrid joint–clinching and adhesive-case study, Appl. Sci. 12 (2022) 11782, https://doi.org/10.3390/app122211782.

[118] S.H. Malene, Y.D. Park, D.L. Olson, Response of exothermic additions to the flux-cored arc welding electrode – part 1. Effectiveness of exothermically reacting magnesium-type flux additions was investigated with the flux cored arc welding process, Weld. J. 86 (2007) 293–302.

[119] Y.D. Park, N. Kang, S.H. Malene, D.L. Olson, Effect of exothermic additions on heat generation and arc process efficiency in flux-cored arc welding, Met. Mater. Int. 13 (2007) 501–509, https://doi.org/10.1007/BF03027910.

[120] H.L. Li, D. Liu, N. Guo, H. Chen, Y.P. Du, J.C. Feng, The effect of alumino-thermic addition on underwater wet welding process stability, J. Mater. Process. Technol. 245 (2017) 149–156, https://doi.org/10.1016/j.jmatprotec.2017.02.023.

[121] B. Trembach, Comparative studies of the three-body abrasion wear resistance of hardfacing Fe-Cr-C-B-Ti alloy, Proc IOP Conf. Ser.: Mater. Sci. Eng. (2023) 1277, https://doi.org/10.1088/1757-899X/1277/1/012016, 012016.

[122] P. Mikolajczak, A. Genau, J. Janiszewski, L. Ratke, Thermo-calc prediction of mushy zone in AlSiFeMn alloys, Metals 7 (2017) 506, https://doi.org/10.3390/met7110506.

[123] I. Barényi, M. Krbaťa, J. Majerík, I. Mikušová, Effect of deformation parameters on microstructure evolution and properties of 33NiCrMoV15 steel, Proc IOP Conf. Ser.: Mater. Sci. Eng. 776 (2020) 012001, https://doi.org/10.1088/1757-899X/776/1/012001.

[124] M.A. Vasylyev, B.N. Morduk, S.M. Voloshko, V.I. Zakiev, A.P. Burmak, D.V. Pefti, Modification of surface layers of Cu–39Zn–1Pb brass at high-frequency impact deformation in the air and argon inert environments, Metallofiz. Noveishie Tekhnol. 42 (2020) 381–400, https://doi.org/10.15407/mfint.42.03.0381.

[125] P. Tyczewski, K. Nadolny, W. Zwierzycki, D. Ulbrich, Studies of simultaneous friction and corrosive processes in the presence of abrasive particles, Materials 15 (2022) 6734, https://doi.org/10.3390/ma15196734.

[126] W. Sawczuk, A. Merkisz-Guranowska, D. Ulbrich, J. Kowalczyk, A.M.R. Cañás, Investigation and modelling of the weight wear of friction pads of a railway disc brake, Materials 15 (2022) 6312, https://doi.org/10.3390/ma15186312.

[127] J. Kowalczyk, D. Ulbrich, K. Sędłak, M. Nowak, Adhesive joints of additively manufactured adherends: ultrasonic evaluation of adhesion strength, Materials 15 (2022) 3290, https://doi.org/10.3390/ma15093290.

[128] A. Stachowiak, D. Wieczorek, K. Gruber, D. Bartkowski, A. Bartkowska, D. Ulbrich, Comparison of tribocorrosion resistance of Inconel® 718 alloy manufactured by conventional method and laser powder bed fusion method, Tribol. Int. 182 (2023) 108368, https://doi.org/10.1016/j.triboint.2023.108368.

[129] V.A. Mechnik, M.O. Bondarenko, V.M. Kolodnitskyi, V.I. Zakiev, I.M. Zakiev, M.O. Kuzin, E.S. Gevorkyan, Influence of diamond–matrix transition zone structure on mechanical properties and wear of sintered diamond-containing composites based on Fe–Cu–Ni–Sn matrix with varying CrB_2 content, Int. J. Refract. Met. Hard Mater. 100 (2021) 105655, https://doi.org/10.1016/j.ijrmhm.2021.105655.

[130] J. Lentz, A. Röttger, W. Theisen, Solidification and phase formation of alloys in the hypoeutectic region of the Fe–C–B system, Acta Mater. 99 (2015) 119–129, https://doi.org/10.1016/j.actamat.2015.07.037.

[131] I. Zakiev, M. Storchak, G.A. Gogotsi, V. Zakiev, Y. Kokoieva, Instrumented indentation study of materials edge chipping, Ceram. Int. 47 (2021) 29638–29645, https://doi.org/10.1016/j.ceramint.2021.07.133.

[132] M. Storchak, I. Zakiev, V. Zakiev, A. Manokhin, Coatings strength evaluation of cutting inserts using advanced multi-pass scratch method, Meas 191 (2022) 110745, https://doi.org/10.1016/j.measurement.2022.110745.

[133] J.H. Kim, K.H. Ko, S.D. Noh, G.G. Kim, S.J. Kim, The effect of boron on the abrasive wear behavior of austenitic Fe-based hardfacing alloys, Wear 267 (2009) 1415–1419, https://doi.org/10.1016/j.wear.2009.03.017.

[134] H. Ohtsuka, Effects of Cu on diffusional transformation behavior and microstructure in Fe–Mn–Si–C steels, ISIJ Int. 379 (1997) 296–301, https://doi.org/10.2355/isijinternational.37.296.

[135] M. Krbata, D. Krizan, M. Eckert, S. Kaar, A. Dubec, R. Ciger, Austenite decomposition of a lean medium Mn steel suitable for quenching and partitioning process: comparison of CCT and DCCT diagram and their microstructural changes, Materials 15 (2022) 1753, https://doi.org/10.3390/ma15051753.

[136] J. Zhang, J. Liu, H. Liao, M. Zeng, S. Ma, A review on relationship between morphology of boride of Fe-B alloys and the wear/corrosion resistant properties and mechanisms, J. Mater. Res. Technol. 8 (2019) 6308–6320, https://doi.org/10.1016/j.jmrt.2019.09.004.

[137] Y.C. Yang, B. Kebe, W.J. James, J. Deportes, W. Yelon, Structural and magetic properties of Y(Mn1−xFex)12, J. Appl. Phys. 52 (1981) 2077–2078, https://doi.org/10.1063/1.329621.

[138] M. Råsander, B. Sanyal, U. Jansson, O. Eriksson, A First Principles Study of the Stability and Mobility of Defects in Titanium Carbide, 2013, p. 2848, https://doi.org/10.48550/arXiv.1303.2848, *arXiv preprint arXiv: 1303.2848*.

[139] N.Y. Filonenko, O.M. Galdina, Effect of carbon on the physical and structural properties of boride Fe_2B, Phys. Chem. Solid State. 17 (2016) 251–255, https://doi.org/10.15330/pcss.17.2.251-255.

[140] I.S. Koifman, T.V. Egorshina, G.V. Laskova, X-ray analysis of borocementite, Met. Sci. Heat. Treat. 11 (1969) 141–142, https://doi.org/10.1007/BF00652283.

[141] N.Yu Filonenko, Investigation of thermodynamic functions of phases containing boron system Fe–B–C, Phys. Chem. Solid State. 12 (2011) 370–374.

[142] F. Mouhat, F.X. Coudert, Necessary and sufficient elastic stability conditions in various crystal systems, Phys. Rev. B 90 (2014) 224104, https://doi.org/10.1103/PhysRevB.90.224104.

[143] R. Islam, M.M. Hossain, M.A. Ali, M.M. Uddin, S.H. Naqib, Metallic boro-carbides of A_2BC (A= Ti, Zr, Hf and W): a comprehensive theoretical study for thermo-mechanical and optoelectronic applications, RSC Adv. 12 (2022) 32994–33007, https://doi.org/10.1039/d2ra05448e.

[144] M. Segall, P.J. Lindan, M. Probert, C.J. Pickard, P.J. Hasni, S. Clark, M. Payne, First-principles simulation: ideas, illustrations and the CASTEP code, J. Phys. Condens. Matter 14 (2002) 2717–2744, https://doi.org/10.1088/0953-8984/14/11/301.

[145] Z.Q. Lv, Z.P. Shi, Y. Li, First-principles study on the structural, electronic and elastic properties of alloyed austenite with Co and Ni, Adv. Mat. Res. 503 (2012) 684–687, https://doi.org/10.4028/www.scientific.net/AMR.503-504.684.

[146] Y. Yang, H. Lu, C. Yu, J.M. Chen, First-principles calculations of mechanical properties of TiC and TiN, J. Alloys Compd. 485 (2009) 542–547, https://doi.org/10.1016/j.jallcom.2009.06.023.

[147] Y. Jian, Z. Huang, X. Liu, J. Sun, J. Xing, Microstructure; mechanical properties and toughening mechanism of directional Fe_2B crystal in Fe–B alloy with trace Cr addition, J. Mater. Sci. Technol. 57 (2020) 172–179, https://doi.org/10.1016/j.jmst.2020.03.058.

[148] X. Wei, Z. Chen, J. Zhong, L. Wang, Y. Wang, Z. Shu, First-principles investigation of Cr-doped Fe_2B: structural, mechanical,; electronic and magnetic properties, J. Magn. Magn Mater. 456 (2018) 150–159, https://doi.org/10.1016/j.jmmm.2018.02.004.

[149] C. Jiang, S. Srinivasan, A. Caro, S. Maloy, Structural, elastic, and electronic properties of Fe_3C from first principles, J. Appl. Phys. 103 (2008) 043502, https://doi.org/10.1063/1.2884529.

[150] A. Gueddouh, B. Bentria, I.K. Lefkaier, First-principle investigations of structure, elastic and bond hardness of Fe_xB (x = 1; 2; 3) under pressure, J. Magn. Magn Mater. 406 (2016) 192–199, https://doi.org/10.1016/j.jmmm.2016.01.013.

[151] M.J. Mehl, B.M. Klein, D.A. Papaconstantopoulos, First principles calculations of elastic properties of metals, Intermet. Compd. Princ. Pract. 1 (1994) 195–210.

[152] J. Yang, Z. Xiao, Z. Li, Q. Wen, F. Yang, First principles study on the structural, electronic and magnetic properties of Ni4C, Comput. Condens. Matter. 1 (2014) 51–57, https://doi.org/10.1016/j.cocom.2014.11.002.

[153] S.Q. Ma, Y. Liu, J.W. Ye, B. Wang, Mechanical properties and electronic structure of N and Ta doped TiC: a first-principles study, Commun. Theor. Phys. 62 (2014) 895, https://doi.org/10.1088/0253-6102/62/6/19.

[154] J.P. Watt, L. Peselnick, Clarification of the Hashin-Shtrikman bounds on the effective elastic moduli of polycrystals with hexagonal,; trigonal, and tetragonal symmetries, J. Appl. Phys. 51 (1980) 1525, https://doi.org/10.1063/1.327804.

[155] C. Chen, L. Liu, Y. Wen, Y. Jiang, L. Chen, Elastic properties of orthorhombic YBa2Cu3O7 under pressure, Crystals 9 (2019) 497, https://doi.org/10.3390/cryst9100497.

[156] C. Chen, L. Liu, Y. Wen, Y. Jiang, L. Chen, Elastic properties of orthorhombic $YBa_2Cu_3O_7$ under pressure, Crystals 9 (2019) 497, https://doi.org/10.3390/cryst9100497.

[157] R. Hill, The elastic behaviour of a crystalline aggregate, Proc. Phys. Soc. 65 (1952) 349–354, https://doi.org/10.1088/0370-1298/65/5/307.

[158] M.I. Naher, S.H. Naqib, First-principles insights into the mechanical; optoelectronic; thermophysical; and lattice dynamical properties of binary topological semimetal $Baga_2$, Results Phys. 37 (2022) 105507, https://doi.org/10.1016/j.rinp.2022.105507.

[159] S.F. Pugh, Relations between the elastic moduli and the plastic properties of polycrystalline pure metals. Lond. Edinb. Dublin Philos *Mag*, J. Sci. 45 (1954) 823, https://doi.org/10.1080/14786440808520496.

[160] I.N. Frantsevich, F.F. Voronov, S.A. Bokuta, Elastic Constants and Elastic Modulus of Metals and Insulators Handbook, Naukova Dumka Publishing House, Kiev, Ukraine, 1983.

[161] M.A. Hadi, M. Roknuzzaman, M.T. Nasir, U. Monira, S.H. Naqib, A. Chroneos, A.K.M.A. Islam, K. Ostrikov, Effects of Al substitution by Si in Ti_3AlC_2 nanolaminate, Sci. Rep. 11 (2021) 3410, https://doi.org/10.1038/s41598-021-81346-w.

[162] X.Q. Chen, H. Niu, D. Li, Y. Li, Modeling hardness of polycrystalline materials and bulk metallic glasses, Intermetallics 19 (2011) 1275–1281, https://doi.org/10.1016/j.intermet.2011.03.026.

[163] S.F. Pugh, Xcii. Relations between the elastic moduli and the plasti properties of polycrystalline pure metals, Lond. Edinb. Dublin Philos. Mag. J. Sci. 45 (1954) 823, https://doi.org/10.1080/14786440808520496.

[164] P. Ravindran, L. Fast, P. Korzhavyi, B. Johansson, Density functional theory for calculation of elastic properties of orthorhombic crystals: application to $TiSi_2$, J App Phys 84 (1998) 4891, https://doi.org/10.1063/1.368733.

[165] D. Sun, u L. Zh, Y. Cai, Y. Yan, F. Ge, M. Shan, Y. Tian, J. Han, Z. Jiang, Tribology comparison of laser-cladded Cr–nFeCoNi coatings reinforced by three types of ceramic (TiC/NbC/B_4C), Surf. Coat. Technol. 450 (2022) 129013, https://doi.org/10.1016/j.surfcoat.2022.129013.

[166] Y. Li, J. Tang, T. Wu, L. Deng, W. Li, L. Wang, H. Deng, W. Hu, X. Zhang, Effect of transition metal atoms on the stacking fault energy and ductility of TiC, Ceram. Int. 47 (2021) 29386–29391, https://doi.org/10.1016/j.ceramint.2021.07.106.

[167] B. Xiao, J.D. Xing, J. Feng, C.T. Zhou, Y.F. Li, W. Su, X.J. Xie, Y.H. Cheng, A comparative study of Cr_7C_3; Fe_3C and Fe_2B in cast iron both from *ab initio* calculations and experiments, J. Phys. D Appl. Phys. 42 (2009) 115415, https://doi.org/10.1088/0022-3727/42/11/115415.

[168] S. Mirosław, Cavitation erosion; abrasive and sliding wear behavior of metal-based structures, Metals 12 (2022) 373, https://doi.org/10.3390/met12030373.

[169] E. Olejnik, J.J. Sobczak, M. Szala, P. Kurtyka, T. Tokarski, A. Janas, Dry sliding; slurry abrasion and cavitation erosion of composite layers reinforced by TiC fabricated in situ in cast steel and gray cast iron, J. Mater. Process. Technol. 308 (2022) 117688, https://doi.org/10.1016/j.jmatprotec.2022.117688.
[170] J. Brezinová, M. Džupon, J. Viňáš, J. Brezina, J. Hašuľ, Analysis of tribodegradation factors limiting the life of the molds, Defect Diffus. Forum 422 (2023) 57–62, https://doi.org/10.4028/p-8qg71v.
[171] S. Knyazev, O. Rebrova, V. Riumin, V. Nikichanov, A. Rebrova, Establishment of structure and operational properties of boried layers on 40X steel obtained from paste by induction heating, Met. Funct. Mater. 28 (2021) 76–83, https://doi.org/10.15407/fm28.01.76.
[172] O.E. Markov, O.V. Gerasimenko, V.V. Kukhar, O.R. Abdulov, N.V. Ragulina, Computational and experimental modeling of new forging ingots with a directional solidification: the relative heights of 1.1, J. Braz. Chem. Soc. 41 (2019) 310, https://doi.org/10.1007/s40430-019-1810-z.
[173] X. Xu, F.H. Ederveen, S. van der Zwaag, W. Xu, Correlating the abrasion resistance of low alloy steels to the standard mechanical properties: a statistical analysis over a larger data set, Wear 368 (2016) 92–100, https://doi.org/10.1016/j.wear.2016.09.014.
[174] J. Archard, Contact and rubbing of flat surfaces, J. Appl. Phys. 24 (1953) 981–988, https://doi.org/10.1063/1.1721448.
[175] A. Leyland, A. Matthews, On the significance of the H/E ratio in wear control: a nanocomposite coating approach to optimised tribological behaviour, Wear 246 (2000) 1–11, https://doi.org/10.1016/S0043-1648(00)00488-9.
[176] K. Johnson, Contact Mechanics, Cambridge University Press, Cambridge; UK, 1985.
[177] J.C. Weaver, Q. Wang, A. Miserez, A. Tantuccio, R. Stromberg, K.N. Bozhilov, P. Maxwell, R. Nay, S.T. Heier, E. DiMasi, D. Kisailus, Insight Analysis of an ultra-hard magnetic biomineral in chiton radular teeth, Mater. Today 13 (2010) 42–52, https://doi.org/10.1016/S1369-7021(10)70016-X.
[178] E.F. Finkin, Examination of abrasion resistance criteria for some ductile metals, J. Lubr. Technol. 96 (1974) 210–214, https://doi.org/10.1115/1.3451924.
[179] S.J. Bull, Using work of indentation to predict erosion behavior in bulk materials and coatings, J. Phys. D Appl. Phys. 39 (2006) 1626, https://doi.org/10.1088/0022-3727/39/8/023.
[180] T.Y. Tsui, G.M. Pharr, W.C. Oliver, C.S. Bhatia, R.L. White, A. Anders, I.G. Brown, Nanoindentation and nanoscratching of hard carbon coatings for magnetic disks, MRS Proc 356 (1994) 767, https://doi.org/10.1557/PROC-383-447.
[181] D. Sun, L. Zhu, Y. Cai, Y. Yan, F. Ge, M. Shan, Y. Tian, J. Han, Z. Jiang, Tribology comparison of laser-cladded CrMnFeCoNi coatings reinforced by three types of ceramic (TiC/NbC/B_4C), Surf. Coat. Technol. 450 (2022) 129013, https://doi.org/10.1016/j.surfcoat.2022.129013.
[182] T.M. Radchenko, V.A. Tatarenko, H. Zapolsky, D. Blavette, Statistical-thermodynamic description of the order–disorder transformation of D019-type phase in Ti–Al alloy, J. Alloys Compd. 452 (2008) 122–126, https://doi.org/10.1016/j.jallcom.2006.12.149.
[183] V.A. Tatarenko, T.M. Radchenko, The application of radiation diffuse scattering to the calculation of phase diagrams of f.c.c. substitutional alloys, Intermetallics 11 (2003) 1319–1326, https://doi.org/10.1016/S0966-9795(03)00174-2.
[184] T.M. Radchenko, O.S. Gatsenko, V.V. Lizunov, V.A. Tatarenko, Martensitic α"-Fe16N2-type phase of non-stoichiometric composition: current status of research and microscopic statistical-thermodynamic model, Prog. Phys. Met. 21 (2020) 580–618, https://doi.org/10.15407/ufm.21.04.580.
[185] I.P. Shatskyi, L.Y. Ropyak, M.V. Makoviichuk, Strength optimization of a two-layer coating for the particular local loading conditions, Strength Mater. 48 (2016) 726–730, https://doi.org/10.1007/s11223-016-9817-5.
[186] L.Ya Ropyak, I.P. Shatskyi, M.V. Makoviichuk, Influence of the oxide-layer thickness on the ceramic–aluminium coating resistance to indentation, Metallofiz. Noveishie Tekhnol. 39 (2017) 517–524, https://doi.org/10.15407/mfint.39.04.0517.
[187] L.Y. Ropyak, I.P. Shatskyi, M.V. Makoviichuk, Analysis of interaction of thin coating with an abrasive using one-dimensional model, Metallofiz. Noveishie Tekhnol. 41 (2019) 647–654, https://doi.org/10.15407/mfint.41.05.0647.
[188] M. Bembenek, M. Makoviichuk, I. Shatskyi, L. Ropyak, I. Pritula, L. Gryn, V. Belyakovskyi, Optical and mechanical properties of layered infrared interference filters, Sensors 22 (2022) 8105, https://doi.org/10.3390/s22218105.
[189] I.P. Shatskyi, M.V. Makoviichuk, L.Ya Ropyak, Equilibrium of laminated Cu/Ni/Cr coating under local load, Nanosistemi, Nanomateriali, Nanotehnologii 21 (2023) 379–389, https://doi.org/10.15407/nnn.21.02.379.
[190] I. Shatskyi, M. Makoviichuk, L. Ropyak, A. Velychkovych, Analytical model of deformation of a functionally graded ceramic coating under local load, Ceramics 6 (2023) 1879–1893, https://doi.org/10.3390/ceramics6030115.